THE ASTROPHYSICAL JOURNAL, 471:211–236, 1996 November 1

ELEMENTAL ABUNDANCE VARIATIONS AND CHEMICAL ENRICHMENT FROM MASSIVE STARS IN STARBURSTS. I. NGC 4214

HENRY A. KOBULNICKY AND EVAN D. SKILLMAN[1]
University of Minnesota, Department of Astronomy, 116 Church Street, SE, Minneapolis, MN 55455; chip, skillman@astro.spa.umn.edu
Received 1996 March 1; accepted 1996 May 31

ABSTRACT

This spectroscopic study of NGC 4214 is part of a project to determine the extent to which the winds and supernovae from massive stars contribute to the *short-term, localized* chemical enrichment of the interstellar medium (ISM) in low-metallicity galaxies. Long-slit optical spectroscopy at 82 distinct spatial locations covering multiple starburst knots reveals no significant *localized* O, N, or He abundance differences that might be attributed to the winds of massive stars. We do find *large-scale* (200 pc) variations in the oxygen abundance. The southernmost, and probably youngest, starburst region exhibits higher O abundances by 0.095 ± 0.019 dex and correspondingly lower N/O (0.108 ± 0.038 dex) than the rest of the bright emission-line regions. This difference is consistent with O pollution at the locations of the young starburst, possibly from recent supernovae. The surveyed regions exhibit an anticorrelation between N/O and O/H consistent with O pollution, but no significant correlations between Ne/O and O/H. If, as expected from nucleosynthesis models, O and Ne are produced predominantly in the same short-lived massive stars, and N is produced predominantly in less massive, longer lived stars, then these trends are both consistent with the O pollution hypothesis. We show that observed internal N/O and O variations within NGC 4214, NGC 5253, and NGC 3125 are consistent with theoretical chemical evolution predictions during a phase of O production associated with massive stars early in a starburst. While uncertainties in the electron temperature, $T(O^{++})$ are the dominant source of error, we show that the observed abundance trends are not consistent with those expected from temperature uncertainty effects. The N/O and He/H ratios are relatively insensitive to temperature errors and should serve as good indicators of abundance inhomogeneities wherever they may exist.

We also present a self-consistent recomputation and tabulation of O, N/O, and He/H measurements in 60 metal-poor H II galaxies from the literature. Analysis of these data indicates that galaxies with strong Wolf-Rayet (W-R) features in their integrated spectrum exhibit identical N/O and He abundances to those galaxies lacking such features. Although abundance pollution from massive stars must occur on long timescales and global spatial scales, we take the absence of significant differences between W-R and non–W-R galaxies as evidence that W-R stars are not a significant contributor to abundance fluctuations on timescales comparable to the lifetimes of the H II regions. Thus, W-R galaxies need not be treated differently than non–W-R galaxies in studies of galactic chemical evolution and primordial abundance studies.

Subject headings: galaxies: abundances — galaxies: individual: NGC 4214 — galaxies: ISM — galaxies: starburst — H II regions — stars: Wolf-Rayet

1. INTRODUCTION

1.1. *On the Role of Nebular Abundance Studies in Galaxies and Chemical Evolution*

Since the recognition of metal-poor H II regions in other galaxies (Peimbert & Spinrad 1970) and the discovery of metal-poor H II regions in dwarf galaxies (Searle & Sargent 1972), studies of the nebular chemical abundances in extragalactic H II regions, principally O, N, and He, have contributed enormously to the understanding of chemical evolution in galaxies and the parameters governing primordial nucleosynthesis in the early universe. Measurements of helium abundances in galaxies with very low metallicity ($O/H < 10^{-4} \equiv 0.12\, Z_\odot \equiv Z < 0.002$; Meyer 1985) have provided the most reliable constraints on the primordial helium mass fraction as a test of cosmological models (Peimbert & Torres-Peimbert 1974, 1976; Lequeux et al. 1979; French 1980; Kinman & Davidson 1981; Kunth & Sargent 1983; Campbell, Terlevich, & Melnick 1986; Pagel et al. 1992; Skillman & Kennicutt 1993). Measurements of oxygen abundances relative to hydrogen (O/H) reveal significant gradients in the disks of large spirals (Searle 1971; Garnett & Shields 1987) but much smaller gradients in barred spirals (Martin & Roy 1994) illustrating the potential importance of gas inflow/outflow in galaxies. Nitrogen (Garnett 1990; Vila-Costas & Edmunds 1993) and carbon (Dufour, Schiffer, & Shields 1984; Dufour 1984; Garnett et al. 1995) abundance determinations as a function of metallicity (O/H) have provided tests for galactic chemical evolution simulations (Tinsley 1974, 1976; Carigi et al. 1995), constrained modeling star formation histories in galaxies, and provided tantalizing observational evidence for metallicity-dependent stellar chemical yields.

In the case of small galaxies where sometimes only a single H II region is observed, it is assumed that the nebular H II region abundances represent the chemical composition of the galaxy ISM as a whole. However, Kunth & Sargent (1986), in an attempt to explain why no galaxies more metal-poor than I Zw 18 (still the current record holder) are seen, suggested that H II regions may "pollute" themselves on short (10^6 yr) timescales with nucleosynthetic products

[1] Currently on sabbatical leave at the Max-Planck-Institut für Astrophysik, Karl-Schwarzschild-Strasse 1, D-85740 Garching, Germany.

from the current burst of star formation. Thus, observed nebular abundances may not reflect the abundance of the gas from which the stars formed or that of the galaxy at large. Pagel, Terlevich, & Melnick (1986) noticed that galaxies with spectral signatures of Wolf-Rayet (W-R) stars (typically broad, 1000 km s^{-1} He II λ4686 emission) often had higher He and N abundances than other galaxies at similar metallicity. They suggested that N-rich and He-rich Wolf-Rayet star winds enrich the nebulae on timescales short compared to the lifetime of the H II region. Since Wolf-Rayet stars are the descendants of only the most massive stars ($M > 35\ M_\odot$; Conti et al. 1983; Humphreys, Nichols, & Massey 1985) that rapidly evolve through heavy mass-loss episodes ($\dot{M} \sim 10^{-5}\ M_\odot\ yr^{-1}$) in 2–3 $\times$ 10^6 yr, the effect of winds may conceivably alter nebular chemical abundances on short timescales, especially in low-metallicity environments in which the differential change in metallicity due to one starburst episode will be dramatic. Evidence for local N and He enrichment is seen in the Galactic W-R shell NGC 6888 (Esteban & Vílchez 1992) and Breysacher 13 in the LMC (Garnett & Chu 1994), while other W-R shells show no sign of enrichment (Esteban et al. 1990). However, the extent to which chemical yields and mass loss depend on initial metallicity is still largely unknown.

At the present time, there exists no deliberate investigation of the effect of massive star winds and supernovae on the short-term abundances in galaxies. The case for localized enrichment is predicated on just a few objects. The galaxy with the best evidence for enrichment is the irregular galaxy NGC 5253. Walsh & Roy (1987, 1989) conducted an optical spectroscopic survey of NGC 5253 and mapped a region showing enhanced N (first noted by Welch 1970) but not showing enhancement in He or in any other elements. They attributed the enhancement to enrichment from W-R star winds. Pagel et al. (1992), in extrapolating the metallicity (O/H) versus He/H relation to zero metallicity to obtain the primordial helium abundance, chose to exclude from their regression analysis those galaxies with W-R features, citing fears that the measured He and N abundances may be contaminated from W-R star winds and not represent global values. Conti (1991) compiled a list of emission-line galaxies with known Wolf-Rayet features and termed some of them "Wolf-Rayet Galaxies" because of their large fraction of W-R stars to O stars. Esteban & Peimbert (1995) modeled the elemental enrichment expected in a sample of 11 H II (mostly Wolf-Rayet) galaxies based on the stellar population in the current burst, an assumed initial mass function, and recent stellar chemical yields. They concluded that elemental enrichment from the current burst cannot self-consistently reproduce the observed O and elevated N and He abundances seen in some W-R galaxies. While the models can easily account for the observed N abundances seen in W-R galaxies, at the same time they underpredict the He and vastly overpredict the O abundances.

This paper is part of a systematic investigation of short-term, localized abundance enrichment by massive stars in young starbursts. Here we present a long-slit spectroscopic mapping of the irregular starburst galaxy NGC 4214, which contains multiple starburst regions, some with strong Wolf-Rayet features. It is thus a good candidate for exhibiting observable localized abundance enrichments, if they exist. Its proximity and similar distance (thus similar plate scale) to NGC 5253, the one well-established case of localized abundance enrichment, make it an ideal target for the search.

1.2. *The Irregular Starburst Galaxy NGC 4214*

NGC 4214, at a heliocentric velocity of 290 km s^{-1}, is a member of the Coma-Sculptor cloud (Tully 1988) and has a distance of 4.1 Mpc (Leitherer et al. 1996 who correct for Galactocentric rotation and Virgocentric infall); this corresponds to a scale of 20.5 pc $arcsec^{-1}$, which we use throughout. Morphologically, it consists of multiple blue starburst regions in the inner 30″ surrounded by a 10′ × 10′ H I disk with a hint of a stellar bar. It is classified as a barred Magellanic irregular (SBmIII; Sandage & Bedke 1994, Plate 330). H I 21 cm observations (Allsop 1979 and references therein; Skillman 1984) reveal an H I mass of 2.4 $\pm$ 0.2 $\times$ $10^9\ M_\odot$, a dynamical mass of 8.0 $\pm$ 0.2 $\times$ $10^9\ M_\odot$, and an extension of neutral hydrogen toward NGC 4190 that lies 29′ (35.6 kpc) to the northwest, which suggests possible tidal interactions.

The multiple starburst knots in the nucleus of NGC 4214 have been the targets of numerous spectroscopic investigations. Talent (1980) and Skillman (1984) presented spectrophotometry of the brightest knots, reported broad He II λ4686 features in some knots, and established that the metallicity of NGC 4214 is less than one-fourth solar ($12 + \log O/H \sim 8.3$). Subsequent spectroscopy (Sargent & Filippenko 1991) established the presence of WC stars and strong Wolf-Rayet features in at least two knots indicating Wolf-Rayet to O star ratios of nearly unity. Recent imaging of the brightest knot with the *Hubble Space Telescope* (Leitherer et al. 1996) showed it contains twice as many O stars as the R136a region in 30 Doradus with an age of 4–5 Myr.

2. OBSERVATIONS AND DATA

2.1. *Observational Parameters*

Long-slit spectra covering the wavelength range 3650–7100 Å were acquired with the GoldCam spectrograph and 3k × 1k CCD on the Kitt Peak 2.1 m telescope[2] on the nights of 1995 January 30–February 2. Conditions were photometric except for the first half of January 30, and seeing averaged 2″+ on January 30 and 1.″0–1.″5 thereafter. The F3KC CCD chip had unexpectedly low sensitivity at short wavelengths as a result of recent coatings designed to reduce fringing in the red. The grating 240, which is blazed at 5500 Å with 500 lines mm^{-1}, was used in first order with a cutoff filter WG360 on January 30, and without a cutoff filter on subsequent nights, to increase the efficiency of the optical system in the blue. When no cutoff filter was used, a small amount of second-order blue leak into the red end of the spectrum required correction as discussed below. The GoldCam focal plane plate scale was 0.″78 $pixel^{-1}$ with a spectral scale of 1.5 Å $pixel^{-1}$. We determined an instrumental resolution (FWHM) of 6.0 Å (January 30) and 4.8 Å (subsequent nights) from the FWHM of lines in He-Ne-Ar calibration lamp. Slit widths were 3.″0 (January 30) and 1.″9 (subsequent nights), and the slit length was 4′.

We observed four positions in NGC 4214, keeping the slit orientation within 20° of the parallactic angle to minimize

[2] Kitt Peak National Observatory and the National Optical Astronomy Observatory is operated by the Association of Universities for Research in Astronomy, Inc. under cooperative agreement with the National Science Foundation.

the effects of light loss outside the slit due to differential atmospheric refraction (Filippenko 1982). Slit locations were chosen to maximize coverage of the bright nebular regions based on the Hα images in Becker et al. (1995) while minimizing offset from parallactic angle. Exposures were 1200 s in duration, short enough that none of the bright continuum regions or strong emission lines saturated the detector. An off-axis autoguider was used for all exposures. Table 1 summarizes the observational parameters for each of the four slit positions which we denote A, B, C, and D. Slit locations are shown in Figure 1 (Plate 5) superimposed on Hα and continuum images of the central portion of NGC 4214 (Hunter 1996). Hα emission is represented in gray scale and the off-Hα continuum in contours. Units are an arbitrary, logarithmic scale. B1950.0 positions are accurate to $\pm 0.5''$ rms. In order to obtain independent data points and increase confidence in the authenticity of any spatial abundance variations detected in this experiment, at least five integrations were obtained at a given location on each night. Each slit position was observed on two separate nights at a different locations on the CCD chip, and each night was calibrated independently.

2.2. *Reductions and Calibration*

The data were reduced in a standard fashion using IRAF. A bias level was subtracted from each frame using the overscan region of the CCD chip. A combination of flat-field images from the night sky and a continuum quartz lamp were divided into each frame to correct for pixel-to-pixel variations along spatial and dispersion axes, respectively. Periodic exposures of a He-Ne-Ar arc lamp served as an absolute wavelength reference and ensured that the wavelength calibration was consistent throughout each night. After wavelength calibration and transformation to equal wavelength intervals along the dispersion axis, images from the same night were combined in groups of three frames of similar air mass with the IRAF combine/crreject algorithm to average frames and reject cosmic-ray events. Air masses never exceeded 1.3. Care was taken to discriminate between cosmic rays and the high peaks of strong emission lines that might also be confused with cosmic-ray events. Tracking with the autoguider was sufficiently good that no shifting or registration of the images was required prior to the combine procedure.

We observed no fewer than five standard stars each night from the list of Oke (1990) at a range of air masses to ensure adequate solutions for extinction and absolute flux calibration. All standards were observed with a wide (8″) slit. In order to judge the magnitude of the second-order blue leak due to removal of the cutoff filter on the latter three nights, we divided standard star spectra from January 30 by spectra from subsequent nights and discovered a small (10%) leakage starting around 6400 Å. The small magnitude of this effect indicates that the falling response of the grating blueward of 3900 Å served rather effectively to cut off second-order blue leak. Nevertheless, a one-dimensional multiplicative correction, constructed from the quotient of standard star frames with and without the cutoff filter, was applied to the standard star frames prior to solving for the instrumental response function.

TABLE 1

OBSERVATIONAL PARAMETERS

Slit	Date	PA (deg)	Slit (arcsec)	Integration Time (s)
A.....	Sep 30	80	3.0	2(3 × 1200)
	Sep 31	80	1.9	2(3 × 1200)
B.....	Feb 1	80	1.9	2(3 × 1200)
	Feb 2	80	1.9	1(3 × 1200)
C.....	Jan 30	150	3.0	2(3 × 1200)
	Jan 31	150	1.9	2(3 × 1200)
D.....	Feb 1	165	1.9	2(3 × 1200)
	Feb 2	165	1.9	1(3 × 1200)

Because of the CCD's low response shortward of 3900 Å, only the two brightest and bluest of the standards, HD 93521 and BD +75°325, could be used in the entire flux calibration, while two additional stars were suitable redward of 4500 Å. Since the solutions from the final three nights were indistinguishable, a common sensitivity function was adopted for them. The number of standard star exposures was sufficient to allow a calculation of atmospheric extinction for each night. This function was quite consistent throughout the run. Source frames were then corrected for atmospheric extinction and flux calibrated using the derived extinction functions and sensitivity functions from the appropriate night. Emission lines from the night sky were subtracted using a linear fit to at least 30 "sky" pixels on either side of the target H II regions. At the redshift of NGC 4214, none of the nebular lines of interest are significantly affected by the presence of nearby night-sky lines or Galactic absorption.

2.3. *Effects of Optical Distortions and Defocusing*

In any long-slit spectroscopy program in which spatially resolved information is a primary objective, one must worry about the effects of optical aberrations in the spatial dimension, as well as changing focus as a function of wavelength. Differences in focus or spatial plate scale as a function of wavelength will compromise the reliability of line ratios from different parts of the spectrum or different locations on the CCD chip. For an experiment such as this one, the effect will be most severe in objects or regions with steep spatial gradients in the nebular surface brightness or when the width of the extraction aperture is small compared to the surface brightness gradient.

To quantify the effects of possible distortions and defocusing, we observed the standard star BD +75°325 at eight spatial positions along the slit in rapid succession. Adding all eight frames together, we fitted Gaussians to the stellar profiles at 44 positions along the dispersion axis, recording the centers and widths. Differences in the instrumental focus (FWHM) as a function of both wavelength and spatial location on the CCD were quantified. The spatial scale at the red end of the spectrum (~7000 Å) was 2.5% larger than at the blue end (~3700 Å). We fitted and applied a geometrical correction to reduce the effects of this barrel distortion before extracting spectra.

2.4. *Extraction of Spectra*

To account for wavelength-dependent atmospheric refraction, we fitted a moderate-order polynomial to make a spatial trace of the stellar continuum present in each exposure, and we constructed apertures for the extraction of one-dimensional spectra. Typically, the shift due to differential refraction did not exceed 2 pixels from the red to blue extremes. The apertures used were 4 pixels (3″, or about twice the typical seeing) wide with 1 pixel of overlap, chosen to maximize signal-to-noise (S/N) ratio while still main-

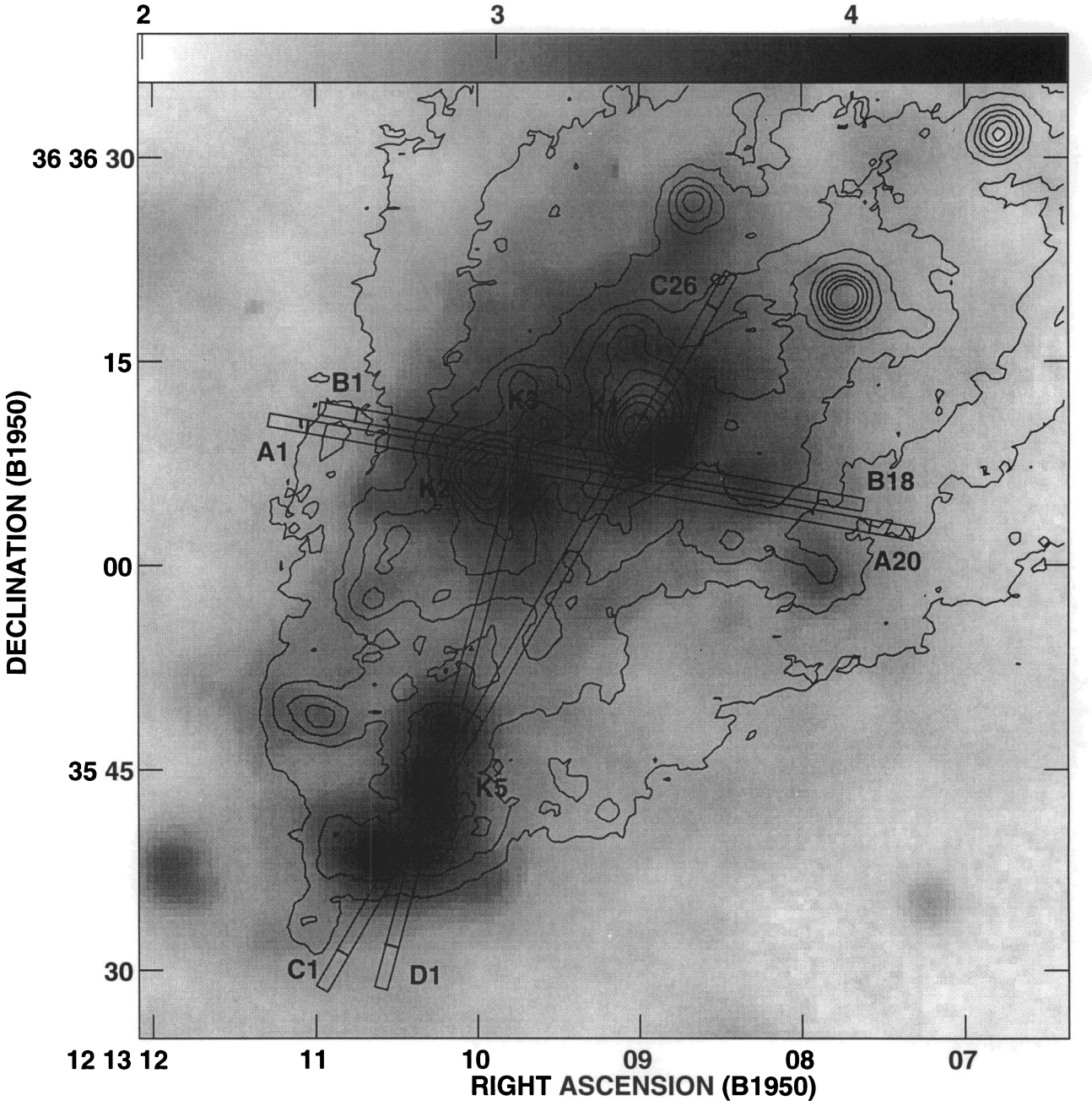

FIG. 1.—Hα (*gray scale*) and 6500 Å continuum (*contours*) image of the central regions of NGC 4214. Intensity is logarithmic, and contours are 20% intervals. Rectangular boxes mark the slit positions for the optical spectroscopy as summarized in Table 1. Coordinates are accurate to ±0″.5 rms. Four continuum knots corresponding to those depicted in Sargent & Filippenko (1991) are labeled, and we add a "Knot 5" to extend their notation.

KOBULNICKY & SKILLMAN (see 471, 213)

taining good spatial resolution. We extracted between 18 and 26 apertures, depending on the slit location, which covered the entire spatial extent of the galaxy where the [O II] λ3727 and [N II] λ6584 lines were strong enough to obtain reliable N^+/O^+ ratios. In most cases the [O II] λ3727 line was the limiting factor because of the poor blue sensitivity of the CCD.

Gaussian profiles were fitted to the prominent emission lines needed for the abundance analysis using the IRAF SPLOT routine. The fitted line fluxes were compared to fluxes by direct integration, and both methods were found to be in good agreement except in the case of the [N II] lines that are partially blended with Hα. We decided to use the Gaussian fitting method throughout.

Occasionally in regions of strong nebular surface brightness, the Hα and [O III] λ4959 and λ5007 lines exhibited broad (10–20 Å) bases that were generally redshifted compared to the narrow portion of the line. Examination of line profiles from the He-Ne-Ar calibration lamp showed no such broad bases, which indicates that they are not the result of instrumental effects but must be intrinsic to NGC 4214. Similar very broad profiles have been seen in other extragalactic H II regions (see the discussion in Skillman & Kennicutt 1993). Where broad components were seen, care was taken to include a second Gaussian component in the fit to obtain accurate total line fluxes. In most cases, errors introduced by neglecting the broad non-Gaussian wings were less than 1%.

In all, this study comprises 292 distinct one-dimensional spectra at 82 spatial locations.

3. DETERMINATION OF PHYSICAL CONDITIONS AND NEBULAR ABUNDANCES

3.1. *Stellar Balmer Absorption and Interstellar Reddening*

We developed a computer program to compute elemental abundance ratios based on emission line strengths. The interactive program first corrects the Balmer lines Hα, Hβ, Hγ, and Hδ for absorption by the underlying stellar population, initially assuming 2 Å EW of absorption. In most cases, 0.5 Å was adopted as a best global value, though in regions of low EW(Hβ), the effects of the underlying stellar absorption are more apparent, and values near 2.0 Å provide better agreement with the observed higher order Balmer line ratios. Each emission line is then corrected for foreground reddening relative to the Hβ line using

$$\frac{I(\lambda)}{I(\mathrm{H}\beta)} = \frac{F(\lambda)}{F(\mathrm{H}\beta)}\, 10^{c(\mathrm{H}\beta)\, f(\lambda)}\,, \tag{1}$$

where I is the true dereddened flux at a given wavelength, F is the observed flux at each wavelength, $c(\mathrm{H}\beta)$ is the logarithmic reddening parameter that describes the amount of reddening relative to Hβ, and $f(\lambda)$ is the wavelength-dependent reddening function (Seaton 1979 as parameterized by Howarth 1983). The value of $c(\mathrm{H}\beta)$ is determined by comparing observed Balmer line ratios to theoretical case B emissivities given by Hummer & Storey (1987) as a function of electron temperature, T_e.

3.2. *Electron Density*

Electron densities are computed using the ratio [S II] λ6716/6731, which is, in all cases, consistent with n_e in the low-density limit such that collisional deexcitation is negligible (Osterbrock 1989) for transitions of interest in this study ([O II] λ3727, [O III] λ5007, λ4959, [N II] λ6548, λ6584). An electron density of 100 ± 50 cm^{-3} is adopted in all cases.

3.3. *Electron Temperatures*

Although the temperature structure inside an H II region may be complex in reality, we adopt the two-temperature zone approximation commonly used consisting of an inner, high-ionization (O^{++}) zone and an outer zone of lower ionization (O^+). The electron temperature, $T_e(O^{++})$, of the high-ionization zone is found, where possible, from the ratio of the [O III] λ4959 + λ5007 line strengths to λ4363 in conjunction with equation (5.4) of Osterbrock (1989). However, positive noise in the vicinity of [O III] λ4363 often mimics a true detection and results in erroneously large values of $T_e(O^{++})$. After an initial reduction of all 292 spectra, we plotted the derived values of T_e and uncertainties versus the S/N in the [O III] λ4363 line in Figure 2. The large scatter and trend toward higher $T_e(O^{++})$ at lower S/Ns are indications that noise spikes near λ4363 are being mistakenly identified as detections. In the high S/N ratio spectra, there is no indication of genuine temperature variations. In order to avoid the well-known tendency to identify noise spikes as λ4363 detections, we adopt a constant electron temperature when the S/N is below a threshold value. Based on Figure 2, we use $T = 10{,}500 \pm 1000$ K in our analyses when the S/N(λ4363) is below 7.

The temperature of the low-ionization zone, $T(O^+)$, is found using a relation between $T_e(O^+)$ and $T_e(O^{++})$ (Pagel et al. 1992; Skillman & Kennicutt 1993) based on photoionization models (Stasińska 1990; Skillman 1989),

$$T_e(O^+) = 2[T_e^{-1}(O^{++}) + 0.8]^{-1} \tag{2}$$

with T_e in units of 10^4 K. We assume

$$T_e(O^{++}) = T_e(He^+) = T_e(Ne^{++}) \tag{3}$$

and

$$T_e(O^+) = T_e(N^+) = T_e(S^+) \tag{4}$$

In a few instances in which [S II] $\lambda\lambda$4068, 4076 are detected, we are able to use the ratio $(I_{6717} + I_{6731})/(I_{4068} + I_{4076})$ to determine directly the electron temperature of the S^+ region. The direct temperature determinations agree well with those based on the approximation from photoionization models, but the S/N of [S II] $\lambda\lambda$4068, 4076 is not high enough to make this method preferable.

Since the amount of underlying stellar Balmer absorption, the reddening, and the electron temperatures in each zone are interdependent, the interactive program solves for these parameters iteratively until a self-consistent solution is obtained.

3.4. *Ionic Abundances*

Abundances by number relative to hydrogen are determined for each ionic species using measured line strengths and emissivities relative to Hβ in the standard manner:

$$\frac{X(\mathrm{A}^{+i})}{X(\mathrm{H}^+)} = \frac{I(\lambda)}{I(\mathrm{H}\beta)}\,\frac{\epsilon(\mathrm{H}\beta)}{\epsilon(\lambda)}\,. \tag{5}$$

Here X is the abundance by number of an ion, A^{+i}, I is the intensity of a given emission line from that ion corrected for extinction relative to Hβ, and ϵ is the emissivity of the line. Hydrogen is assumed to be completely ionized so that

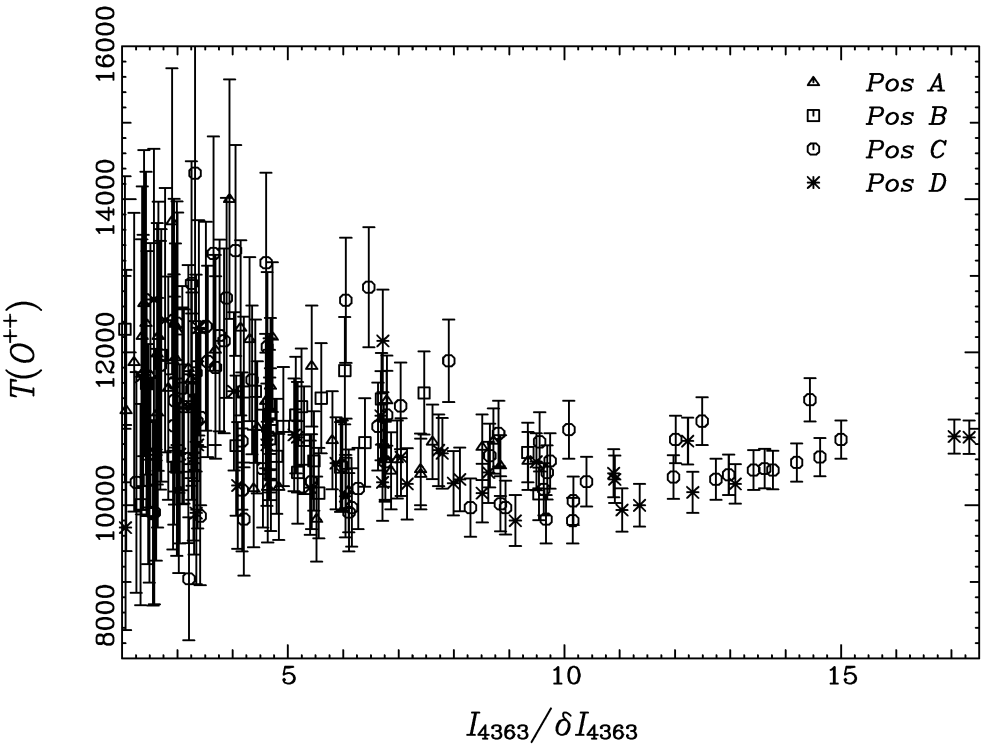

FIG. 2.—Derived electron temperature, $T_e(O^{++})$ vs. the signal-to-noise ratio of the [O III] λ4363 line. The large scatter and trend toward higher T_e at lower signal-to-noise ratio are indications that noise spikes near λ4363 may easily be mistaken for detections. In our abundances analyses, we adopt a constant electron temperature of 10,500 K when the S/N is below 7.

the abundance of an ion relative to H^+ gives the total abundance relative to hydrogen. Theoretical emissivities for the forbidden lines are computed using the five-level atom program of De Robertis, Dufour, & Hunt (1987) with updated collision strengths (Shaw & Dufour 1995). Helium emissivities are computed from a power-law fit to the theoretical emissivities of Smits (1996) between 5000 and 20,000 K:

$$\epsilon(\lambda 4471) = 5.187 \times 10^{-22} T_e^{-0.984}, \quad (6)$$

$$\epsilon(\lambda 5876) = \epsilon(\lambda 4471) \times 7.966 T_e^{-0.116}, \quad (7)$$

$$\epsilon(\lambda 6678) = \epsilon(\lambda 4471) \times 2.598 T_e^{-0.131}. \quad (8)$$

We calculate ionic abundances for O^+ and O^{++} using the λ3727 and λ5007 lines, respectively. O^{+++} abundances are from

$$\frac{O^{+++}}{H^+} = \frac{He^{++}}{He^+}\left[\frac{O^{++}+O^+}{H^+}\right] = \frac{I(\lambda 4686)}{I(\lambda 5876)}\frac{\epsilon(\lambda 5876)}{\epsilon(\lambda 4686)}\left[\frac{O^{++}+O^+}{H^+}\right]. \quad (9)$$

We calculate ionic abundances for S^+ and S^{++} using the $\lambda\lambda$6717/31 and λ6312 lines, respectively, while He^+ and He^{++} are based on the λ5876 and λ4686 lines. Ne^{++} is computed from λ3868, and N^+/O^+ is based on

$$\frac{N^+}{O^+} = \frac{I(\lambda 6584)}{I(\lambda 3727)}\frac{\epsilon(\lambda 3727)}{\epsilon(\lambda 6584)}. \quad (10)$$

Total elemental abundances, relative to H, are obtained by summing over all ionization states and, in some cases, by multiplying by an ionization correction factor to account for ionization states without observed emission lines. The expressions used are

$$\frac{O}{H} = \frac{O^+}{H^+} + \frac{O^{++}}{H^+} + \frac{O^{+++}}{H^+} \quad (11)$$

$$\frac{S}{H} = \left[\frac{S^+}{H^+} + \frac{S^{++}}{H^{++}}\right] \times \mathrm{ICF}(S^{+++}), \quad (12)$$

where $\mathrm{IFC}(S^{+++})$ is computed from equation (4) of Garnett (1989) with $\alpha = 2.5$, which represents a best fit to the photoionization models presented in his Figure 7:

$$\frac{He}{H} = \frac{He^+}{H^+} + \frac{He^{++}}{H^+}, \quad (13)$$

$$\frac{N}{O} = \frac{N^+}{O^+}, \quad (14)$$

$$\frac{Ne}{H} = \frac{Ne^{++}}{H^+} \times \mathrm{ICF}(Ne) = \frac{Ne^{++}}{H^+}\frac{O}{O^{++}}. \quad (15)$$

Equation (14) appears justified in low-metallicity environments in which photoionization models indicate uncertainties of less than 20% through this approximation (Garnett 1990). For He, no correction has been applied for collisional excitation effects that are expected to be negligible (<1%) in low-temperature, low-density environments such as NGC 4214 (Clegg 1987).

The [O I] λ6300 line has been shown by Skillman (1985) to be a sensitive indicator of the presence of shocks due to supernovae remnants within giant H II regions. Where detected with sufficient S/N, the λ6300/Hβ ratio ranges

between 0.01 and 0.07, in good agreement with the range found in photoionization models of metal-poor H II regions (Stasińska 1990). Thus, the effect of shocks artificially raising our electron temperature measurements (see the discussion in Peimbert, Sarmiento, & Fierro 1991) is not likely to be important. When detected, the lines of neutral N and O probably arise at the neutral interface of the H II regions and are not considered in our abundance analysis. In any case, adding the contribution from these species raises the O and N abundances by less than 2% even where [O I] and [N I] lines are most prominent.

3.5. *Uncertainties*

Uncertainties on the emission-line strengths were calculated based on the number of accumulated electrons in each pixel in a manner similar to that of Skillman & Kennicutt (1993). The fractional error on a given emission line is

$$\frac{\delta L}{L} = \{\sigma_{C1}^2 + \sigma_{C2}^2 + \sigma_{\rm sky}^2 + \sigma_{\rm rdn}^2 + \sigma_{C(\rm H\beta)}^2 + \sigma_{\rm ff}^2 + \sigma_{\rm sen}^2\}^{1/2} L^{-1} \quad (16)$$

$$= \{C_1 + C_2 + (n_0/\sqrt{n_s})S + nAN^2 + [2.3f(\lambda)\delta c(\rm H\beta)L]^2 + (0.01L)^2 + (\delta FL)^2\}^{1/2} L^{-1} . \quad (17)$$

Here σ_{C1}, σ_{C2}, $\sigma_{\rm sky}$, $\sigma_{\rm rdn}$, $\sigma_{C(\rm H\beta)}$, $\sigma_{\rm ff}$, and $\sigma_{\rm sen}$ are, respectively, the uncertainties due to Poisson noise on the line plus continuum, continuum subtraction, sky subtraction, readnoise, reddening, flat-fielding, and flux calibration. L is the total number of electrons in the emission line; C_1 is the sum of electrons in the line, sky, and continuum; C_2 is the number of electrons in the continuum; n_0 is the number of CCD rows summed in the extracted spectrum; n_s is the number of CCD rows averaged in the sky subtraction process; S is the average sky background in a single column; n is the number of integrations averaged to construct the final spectrum; A is the number of pixels summed for a given emission line; N is the rms readout noise, which was 8.5 electrons; $\delta c(\rm H\beta)$ is the uncertainty in the reddening parameter; and δF is the rms error in the fit to the sensitivity function during flux calibration, which is 0.015 mag. In most cases, the Balmer lines are strong enough that $\delta c(\rm H\beta)$ is constant at 0.04, and it is determined almost entirely by the rms in the flux calibration. The sixth term in the above expression accounts for flat-fielding uncertainties, estimated to be 1%.

The uncertainties in the emission-line strengths were then propagated into uncertainties in the derived ionic abundances by a 5000 iteration Monte Carlo simulation that adds Gaussian noise to the line strengths and recomputes new ionic abundances in the manner described above, taking into account the uncertainties of the line strengths on the derived electron temperature and ionic emissivities. The rms of the resulting abundance distribution is quoted as the formal uncertainty in our tabulated ionic abundances.

4. THE DATA AND RESULTS

4.1. *Spatial Variations of the Physical Parameters: General Trends*

The number of apertures for each slit is limited by the size of the region with detectable [O II] λ3727. Slit positions A, B, C, and D were divided into 20, 18, 26, and 18 apertures, respectively. Apertures are identified by the letter indicating the slit position in Figure 1, and a number indicating the location along the slit A1, A2, ..., C1, C2, ..., etc). In most cases, there are two spectra from each of two consecutive nights. This provides three or four independent data points at each spatial location that can be used to assess the repeatability of the resulting abundances and the appropriateness of the stated uncertainties.

Figure 3 shows physical parameters across each of the four slit positions. Parameters included in the plot are as follows:

1. The logarithm of the stellar continuum flux at Hβ (ergs s^{-1} cm^{-2} $Å^{-1}$).
2. The logarithm of the Hβ flux (ergs s^{-1} cm^{-2}).
3. The emission equivalent width of Hβ in Å.
4. The logarithmic reddening parameter, $c(\rm H\beta)$.
5. The derived electron temperature in the [O III] zone, $T_e(O^{++})$.
6. The dereddened [O II] λ3737 flux relative to the Hβ flux.
7. The dereddened [N II] λ6584 flux relative to the Hβ flux.
8. The logarithm of the N/O abundance ratio.
9. The He/H abundance ratio.
10. The logarithm of the abundance of singly ionized oxygen to hydrogen.
11. The logarithm of the abundance of doubly ionized oxygen to hydrogen.
12. 12 + the logarithm of the O/H abundance ratio.

Symbols distinguish data from different nights and also distinguish independent spectra from the same night. See the figure legend for details. Error bars are centered on the weighted mean of the individual data points, and their separation indicates the typical 1 σ uncertainty (not the error of the mean). The x-axis indicates the distance in arcseconds from the labeled end of the rectangular slit markers in Figure 1. Positions with strong, broad emission in the vicinity of 4686 Å indicative of Wolf-Rayet stars are denoted in the top panel with a capital W. Positions with marginal evidence for broad emission are denoted with lowercase w.

4.1.1. *Agreement from Night to Night*

Visual inspection of Figure 3 shows that agreement of stellar continuum and Hβ spatial profiles between spectra taken on different nights is generally quite good and that agreement between different spectra from the same night is even better. In the case of positions A and C, this agreement is especially remarkable given that a wider (3.″0) slit width was used on January 30 than on January 31. The most significant discrepancies occur at position C near location C20, the strong continuum peak containing Wolf-Rayet stars (Knot 1 of Sargent & Filippenko 1991). As will be shown later, this does not appear to influence significantly the results of abundance calculations in these regions. Note also that in the vast majority of cases, the data points at a given position fall well within the error bars, which indicates that the repeatability is good from night to night.

The one quantity that shows considerable variation from position to position and from night to night is the logarithmic reddening parameter, $c(\rm H\beta)$. Variations are strongest for slit positions A and C, which involved different slit widths on consecutive nights. This is probably evidence for small-scale variations in reddening and optical depth. We plotted $c(\rm H\beta)$ versus the EW(Hβ) and found no correlation,

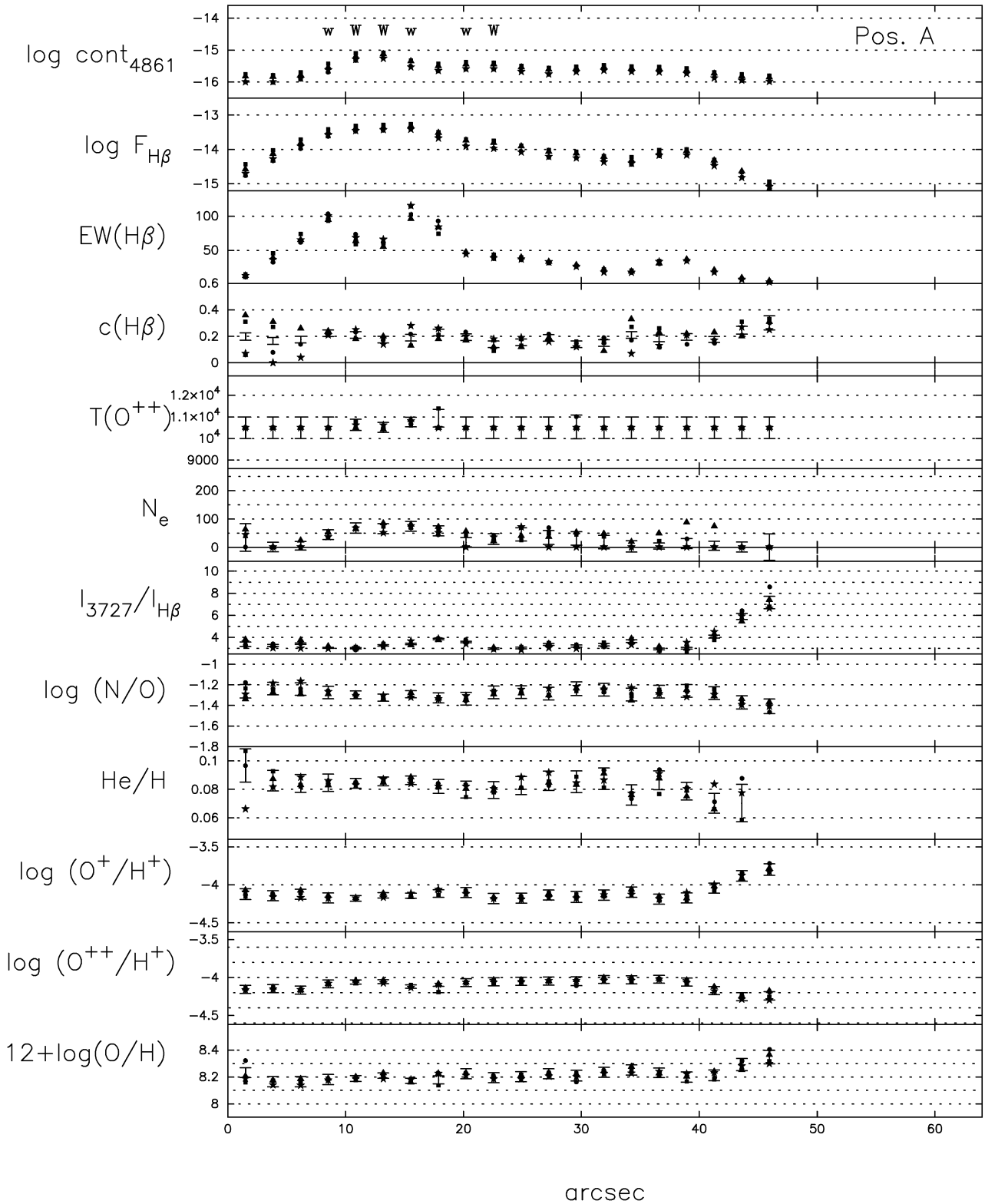

FIG. 3.—Physical parameters for spatial locations across each slit position. Horizontal serifs are centered on the weighted mean of the four data points, and their separation indicates the 1 σ uncertainty. The x-axis indicates the distance in arcseconds from the labeled end of the rectangular slit markers in Fig. 1. (*a*) Filled triangles and squares represent data from separate observations from January 30, while filled circles and stars denote data from separate observations on January 31; (*b*) triangles and squares denote February 1, and filled circles denote February 2; (*c*) triangles and squares denote January 30, and circles and stars denote January 31; (*d*) triangles and squares denote February 1, and filled circles denote February 2. A capital W denotes locations of strong W-R features, while a lowercase w denotes weak W-R features.

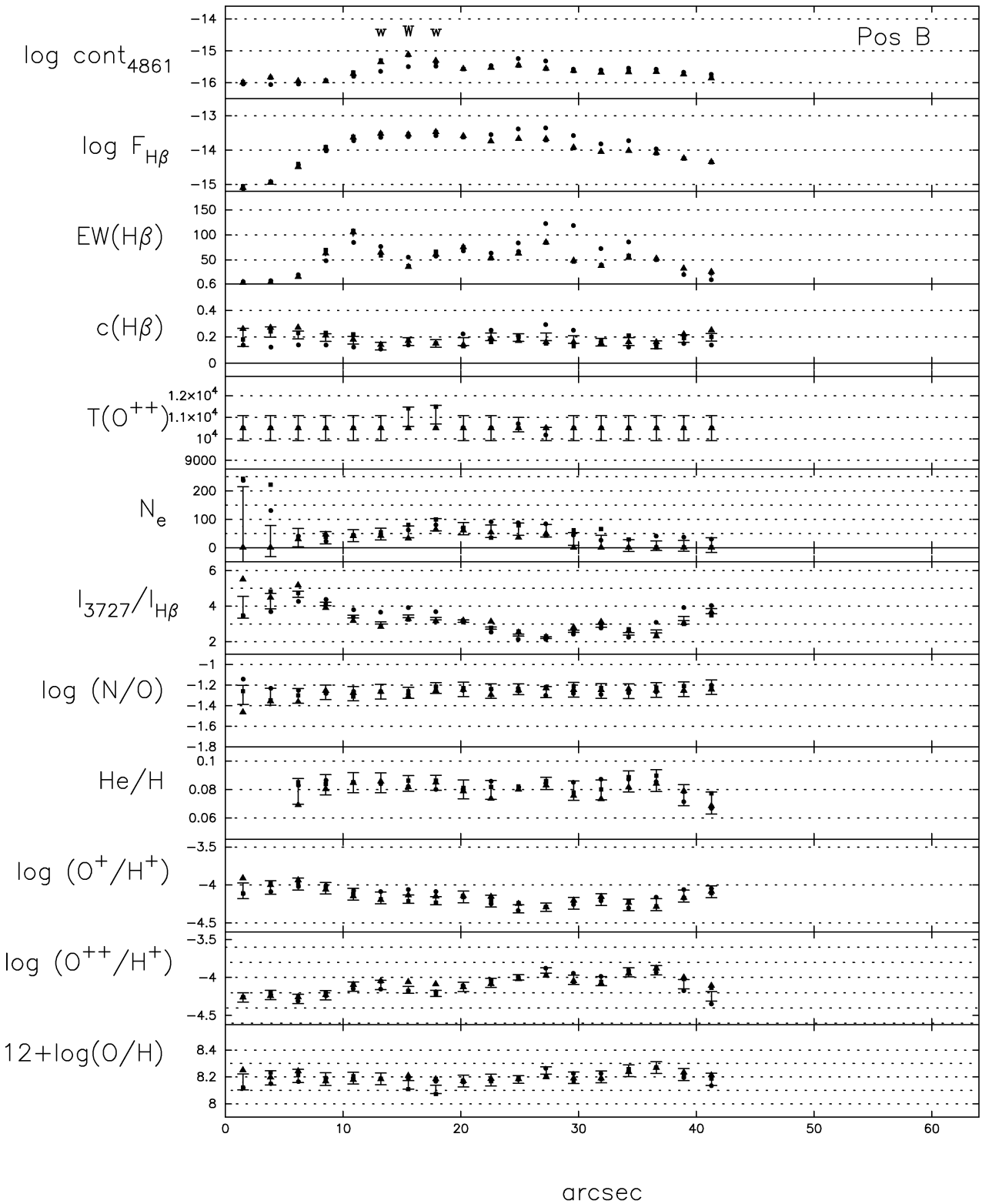

FIG. 3—*Continued*

although one might be expected if dust and extinction were preferentially associated with the molecular gas and star formation.

4.2. *Individual Slit Positions*

4.2.1. *Position A*

Slit position A (see Fig. 3*a*) passes close to the four continuum knots studied by Sargent & Filippenko (1991), but south of the strongest continuum peak, Knot 1 in their notation. W-R features are noted at positions A4–A7 and A9–A10 along the slit. The [O III] λ4363 line is strong enough at only three locations to measure directly the electron temperature. No appreciable abundance differences are noted along the slit.

Figure 4 shows a representative spectrum extracted from position A6, including the obvious W-R features. This

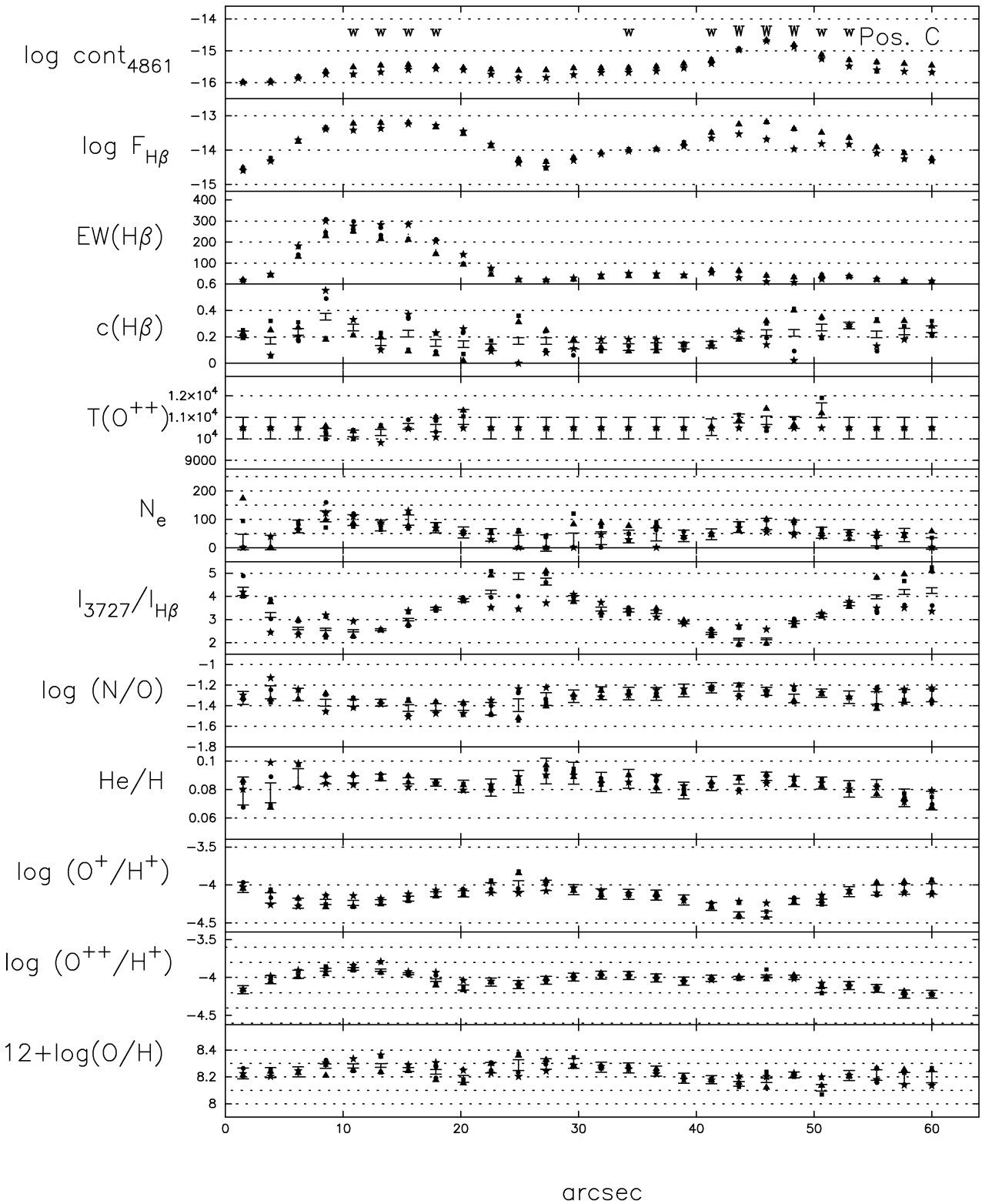

FIG. 3—*Continued*

region corresponds most nearly to Sargent & Filippenko's Knot 2. The spectrum in Figure 4 is characterized by a rising blue continuum with prominent broad emission near 4686 Å commonly seen in the winds of WN stars, with narrow emission from [Fe III], He II, and [Ar IV]. Another broad bump is present near 5800 Å and is due to [C IV] λλ5801, 5812 from Wolf-Rayet WC subclass stars.

The line strengths and uncertainties for this aperture are listed in Table 2. The derived ionic abundances and uncertainties are found in Table 3. To illustrate the magnitude of each source of uncertainty in line strengths, we have explicitly listed the contribution from each term in equation (17). In most cases, Table 2 shows that the uncertainties in $c(\mathrm{H}\beta)$ dominate the error budget for strong lines, followed by the

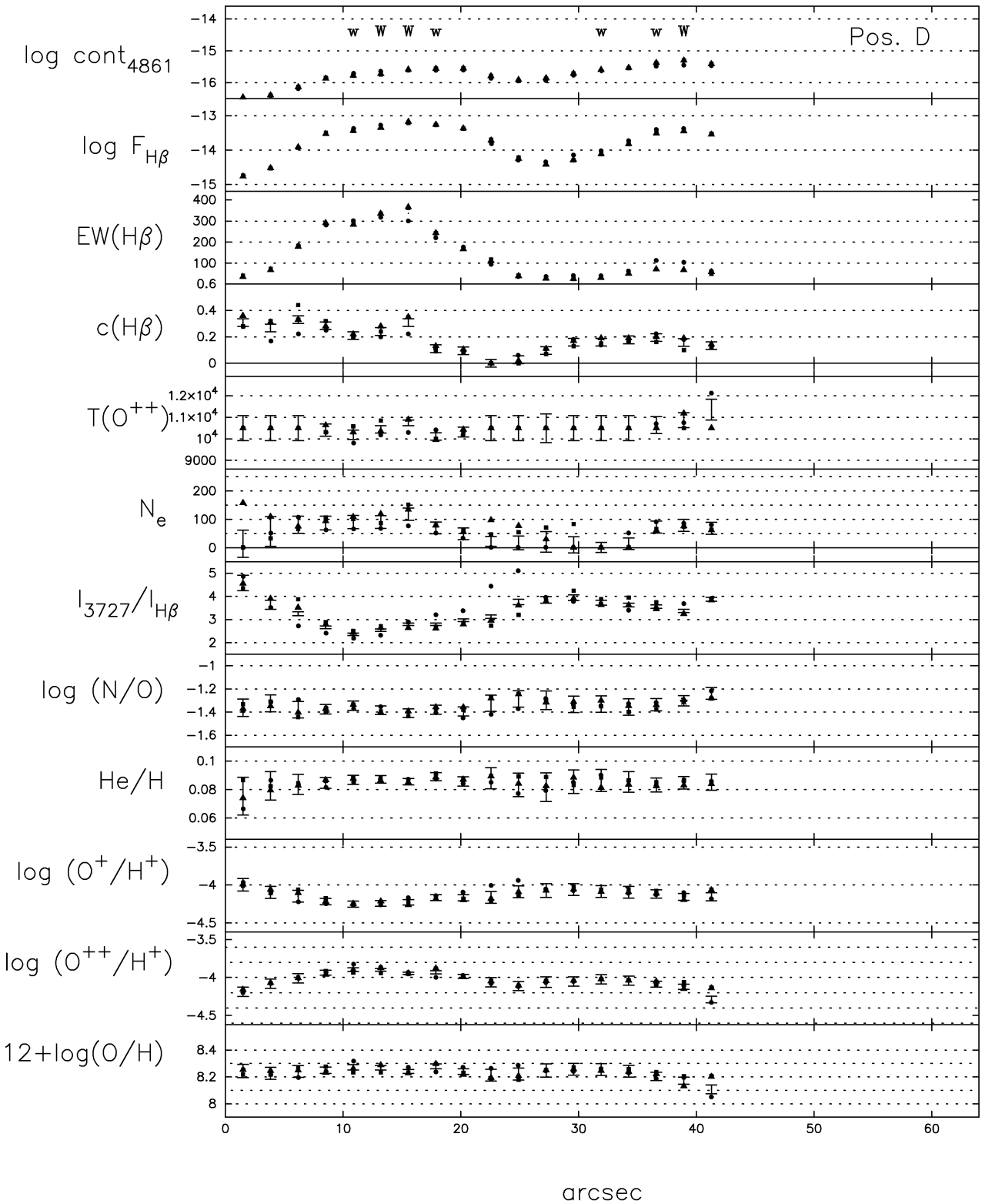

FIG. 3—*Continued*

uncertainties due to Poisson noise, which becomes more important for weaker lines. Readnoise becomes significant for the very weakest lines.

4.2.2. *Position B*

Slit position B, shown in Figure 3*b*, lies parallel to and just north of position A and contains only weak Wolf-Rayet features. No abundance variations with position are evident.

4.2.3. *Position C*

Position C, shown in Figure 3*c*, traverses two starburst regions, including the one with strong Wolf-Rayet features denoted Knot 1 by Sargent & Filippenko (1991), further

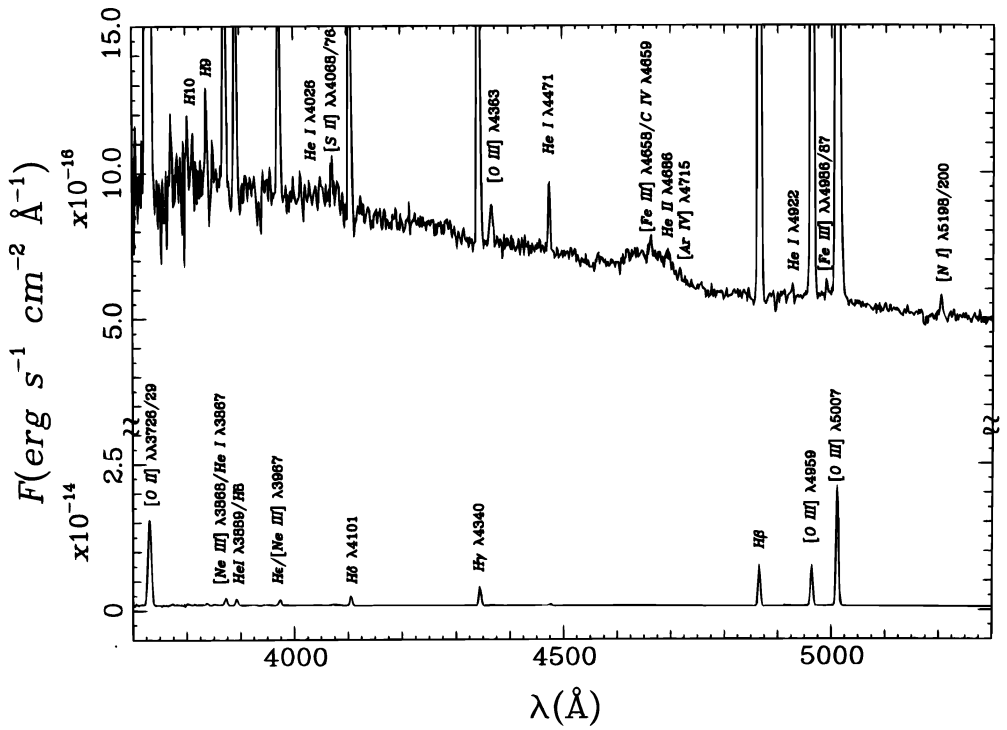

FIG. 4*a*

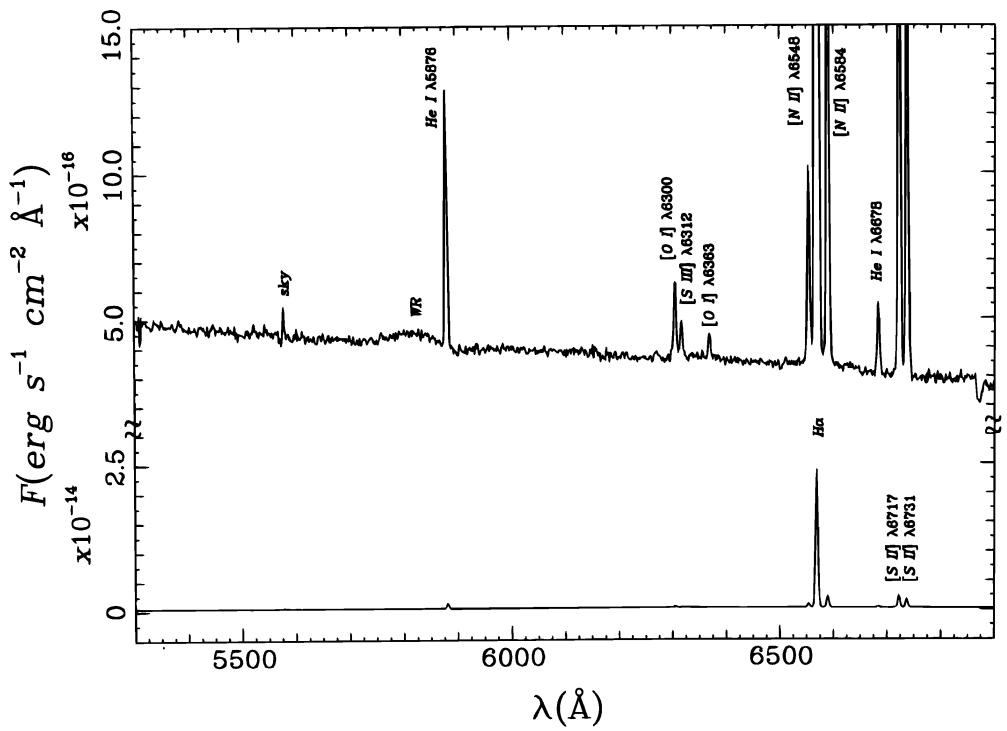

FIG. 4*b*

FIG. 4.—Spectrum from aperture A6. (*a*) Blue, (*b*) red. Note broad W-R features near 4686 Å and 5800 Å and a rising continuum in the blue.

studied by Leitherer et al. (1996). The southern region with strong Hα emission we will denote "Knot 5" to extend the notation of Sargent & Filippenko (1991). Knots 5 and 1 are centered roughly at positions C6 and C20, respectively; both contain W-R features and appear to exhibit real abundance differences, with Knot 1 having lower O/H and higher N/O.

Spectra for apertures C6 and C20, representing these two regions, are shown in Figure 5 and Figure 6. The spectrum in Figure 5 is similar to that in Figure 4 from Knot 2 in terms of its weak but blue continuum and obvious [N I] and [O I] lines. The broad W-R bumps near 4686 Å and 5800 Å, however, are almost nonexistent, but the narrow [Fe III] λ4658, He II λ4686, and [Ar IV] λ4715 lines indica-

TABLE 2

POSITION A6: LINE STRENGTHS

Line	$\frac{I_0}{I_{H\beta}}$	σ_{C1}	σ_{C2}	σ_{sky}	σ_{rdn}	$\sigma_{c(H\beta)}$	σ_{ff}	σ_{sen}
3727 [O II]	3.172 ± 0.114	0.028	0.003	0.000	0.023	0.091	0.032	0.048
3868 [Ne III].....	0.198 ± 0.013	0.005	0.002	0.000	0.010	0.005	0.002	0.003
4068 [S II]	0.015 ± 0.003	0.001	0.000	0.000	0.002	0.001	0.000	0.000
4076 [S II]	0.008 ± 0.003	0.001	0.000	0.000	0.001	0.001	0.000	0.000
4101 Hδ.....	0.246 ± 0.008	0.003	0.001	0.000	0.004	0.005	0.002	0.004
4340 Hγ.....	0.479 ± 0.012	0.004	0.001	0.000	0.003	0.007	0.005	0.007
4363 [O III].....	0.021 ± 0.003	0.001	0.001	0.000	0.003	0.000	0.000	0.000
4471 He I	0.030 ± 0.003	0.001	0.001	0.000	0.002	0.000	0.000	0.000
4686 He II.....	0.003 ± 0.002	0.001	0.001	0.000	0.002	0.000	0.000	0.000
4861 Hβ.....	1.000 ± 0.019	0.005	0.001	0.000	0.002	0.000	0.010	0.015
4969 [O III].....	0.938 ± 0.018	0.004	0.001	0.000	0.002	0.003	0.009	0.014
5007 [O III].....	2.808 ± 0.052	0.007	0.001	0.000	0.001	0.011	0.028	0.042
5876 He I	0.110 ± 0.004	0.001	0.000	0.000	0.001	0.003	0.001	0.002
6312 [S III]	0.016 ± 0.002	0.036	0.021	0.002	0.073	0.035	0.010	0.015
6548 [N II]	0.084 ± 0.004	0.001	0.000	0.000	0.001	0.003	0.001	0.001
6564 Hα.....	2.846 ± 0.122	0.006	0.000	0.000	0.001	0.111	0.028	0.043
6584 [N II]	0.249 ± 0.011	0.002	0.000	0.000	0.001	0.010	0.002	0.004
6678 He I	0.029 ± 0.002	0.001	0.000	0.000	0.001	0.001	0.000	0.000
6717 [S II]	0.253 ± 0.012	0.002	0.000	0.000	0.001	0.010	0.003	0.004
6731 [S II]	0.182 ± 0.009	0.002	0.000	0.000	0.001	0.008	0.002	0.003
$c(H\beta)$	0.17 ± 0.04							
$F(H\beta)$ ($\times 10^{14}$).....	3.7 ± 0.1							
EW(Hβ).....	61 ± 1							
n_e (cm^{-3}).....	≤100.							

tive of hot stars are present. Figure 1 shows that while Knot 5 exhibits strong Hα emission, the continuum component is almost entirely absent. Based on the Hα/continuum images in Figure 1, the EW(Hα) in the vicinity of Knot 5 is very large. This suggests a very young starburst dominated by massive stars and intense UV radiation fields. Figure 6 from position C20 (Knot 1) displays a strong blue stellar continuum with broad W-R features at 4686 Å and 5800 Å. The H and He emission lines are seen here in absorption. The strong optical continuum and presence of broad W-R features suggests a more evolved burst than the one in Knot 5. Line ratios and abundances at positions C6 and C20 are given in Table 3 and Table 4. The oxygen abundances (12 + log [O/H]) at positions C6 and C20 are $8.36^{+0.03}_{-0.04}$ and $8.20^{+0.08}_{-0.09}$, respectively, while log (N/O) is $-1.38^{+0.08}_{-0.09}$ and $-1.26^{+0.12}_{-0.17}$.

In order to quantify these abundance differences better with better S/N, we extracted spectra from position C using a 12.5″ (4 times larger) aperture at 9″ intervals. The resulting across-the-slit diagram is shown in Figure 7. This plot agrees well with the same data at higher spatial resolution from Figure 3*c* and the S/N is better, which confirms the abundance differences between Knots 1 and 5. In general, the entire southern half of the surveyed region exhibits higher O/H and lower N/O than the rest of the galaxy. This trend is also seen in spectra at position D.

4.2.4. *Position D*

Slit position D shown in Figure 3*d* crosses Knot 5 in the southern portion of the surveyed region and passes near Knots 2 and 3 as well. The lower N/O in the vicinity of Knot 5 (locations C4–C9) compared to the rest of the

TABLE 3

DERIVED PARAMETERS AND ABUNDANCES

Parameter	Position A6	Position C6	Position C20
$T(O^{++})$ (K)	10400 ± 500	9800 ± 300	10500 ± 1000
$T(O^{+})$ (K)	11400 ± 700	11000 ± 600	11400 ± 1100
$T(S^{+})$ (K)	10100 ± 1300	11050 ± 1100	<14300
O^{+}/H^{+} ($\times 10^5$)	7.16 ± 1.42	6.64 ± 1.17	5.75 ± 1.76
O^{++}/H^{+} ($\times 10^5$)	9.07 ± 1.15	16.23 ± 1.41	10.03 ± 2.47
O^{+++}/H^{+} ($\times 10^5$).....	0.04 ± 0.04	0.30 ± 0.07	0.12 ± 0.08
O/H ($\times 10^5$).....	16.28 ± 1.83	23.17 ± 1.83	15.90 ± 3.04
12 + log (O/H)	$8.21^{+0.05}_{-0.05}$	$8.36^{+0.03}_{-0.04}$	$8.20^{+0.08}_{-0.09}$
S^{+}/H^{+} ($\times 10^7$).....	7.47 ± 1.42	5.29 ± 1.00	6.54 ± 1.56
S^{++}/H^{+} ($\times 10^7$)	32.10 ± 3.59	43.98 ± 4.93	27.97 ± 9.31
S^{++++}/H^{+} ($\times 10^7$)	4.46 ± 1.54	12.39 ± 2.54	5.88 ± 2.98
S/H ($\times 10^7$)	44.02 ± 2.33	61.65 ± 3.41	40.39 ± 3.94
log (S/O)	$-1.57^{+0.04}_{-0.04}$	$-1.57^{+0.03}_{-0.04}$	$-1.60^{+0.08}_{-0.10}$
N^{+}/O^{+}	0.05 ± 0.01	0.04 ± 0.01	0.06 ± 0.02
log (N/O).....	$-1.344^{+0.081}_{-0.100}$	$-1.377^{+0.077}_{-0.093}$	$-1.258^{+0.122}_{-0.170}$
Ne^{++}/O^{++}	0.153 ± 0.031	0.134 ± 0.019	0.208 ± 0.079
log (Ne/O).....	$-0.81^{+0.08}_{-0.10}$	$-0.87^{+0.06}_{-0.07}$	$-0.68^{+0.14}_{-0.21}$
He^{+}/H^{+}	0.085 ± 0.007	0.089 ± 0.005	0.084 ± 0.012

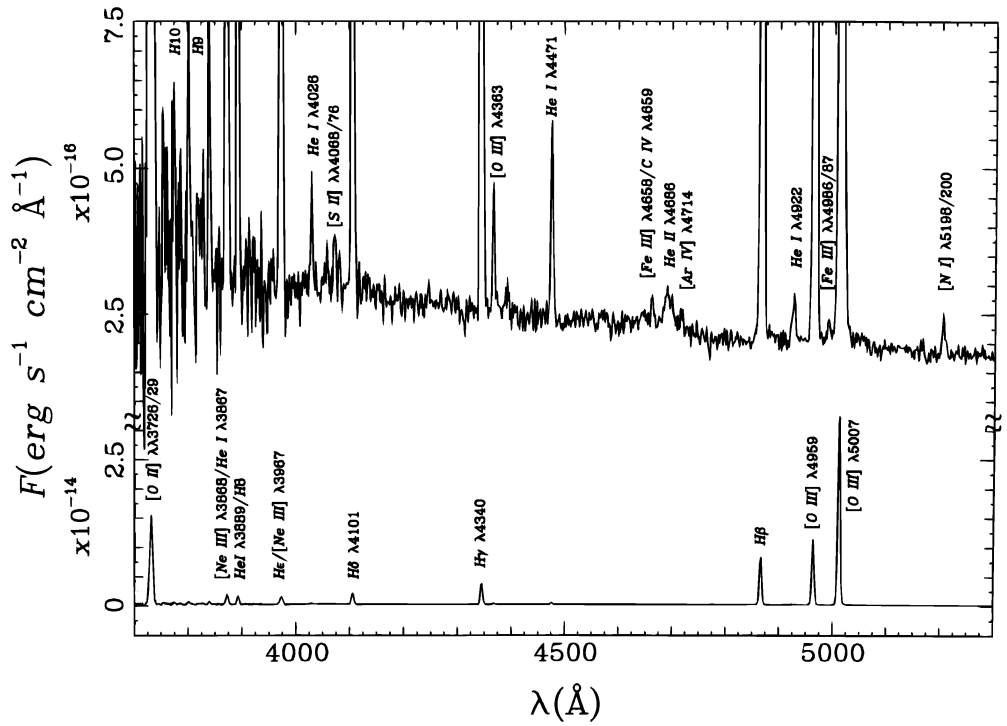

FIG. 5*a*

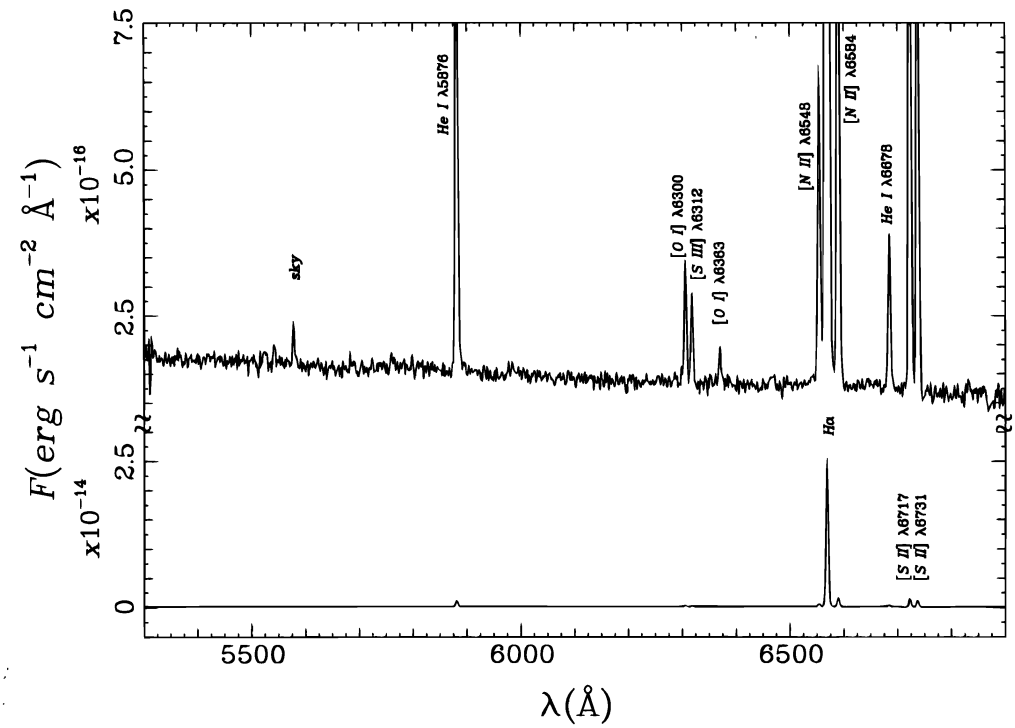

FIG. 5*b*

FIG. 5.—Spectrum from aperture C6. (*a*) Blue, (*b*) red. Note predominantly narrow features near 4686 Å and a relatively weak continuum.

galaxy is confirmed here in locations D4–D9, although the λ4363 line is weak and electron temperatures are assumed to be 10,500 K at many locations. Nevertheless, extractions with wide (12″.5) apertures similar to Figure 7 do detect λ4363 with a high enough S/N to compute T_e directly and to confirm that the abundance differences between Knot 5 and the rest of the galaxy appear to be genuine.

4.3. *Abundance Diagnostics and Large-Scale Abundance Variations*

The single largest source of uncertainty in computing abundances is due to uncertainties in the ionic emissivities driven by the uncertainty in electron temperatures. It is not always easy to distinguish true abundance fluctuations from

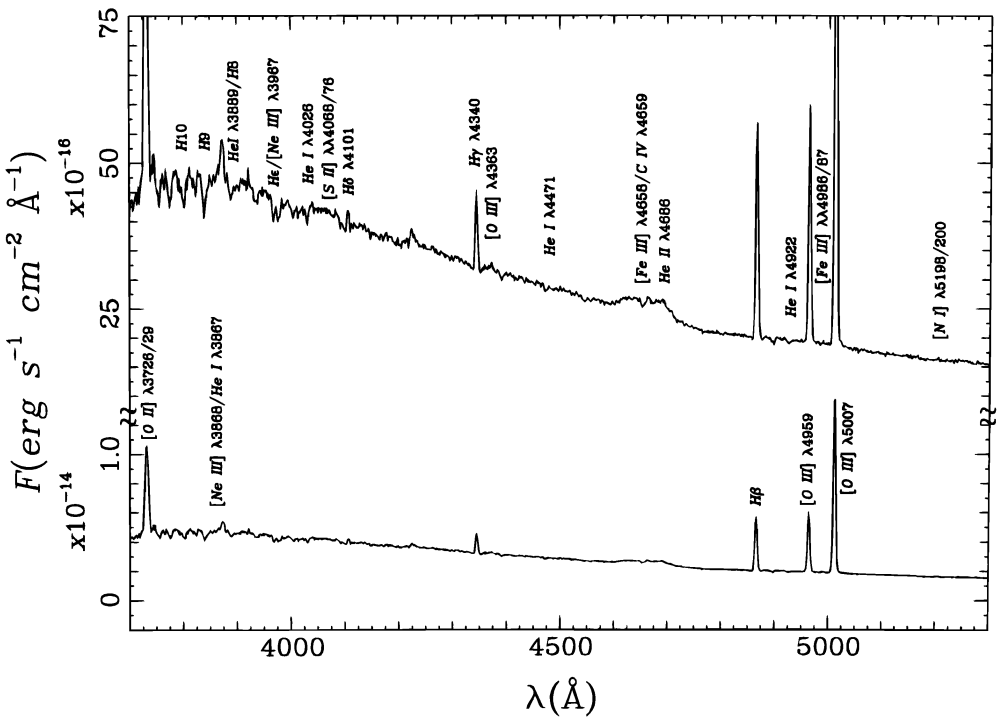

FIG. 6a

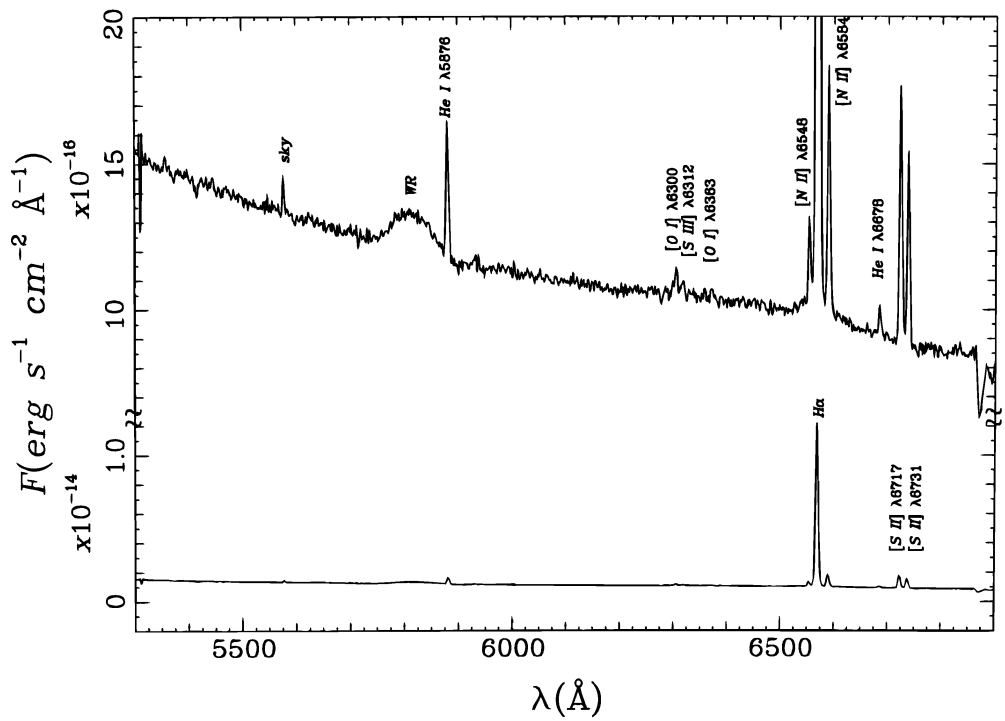

FIG. 6b

FIG. 6.—Spectrum from aperture C20 corresponding to Knot 1 of Sargent & Filippenko (1991). (*a*) Blue, (*b*) red. Note strong, broad W-R features and that He lines and high-order Balmer lines are seen in absorption.

temperature fluctuations or the misleading effects of systematic errors in temperature determination. Systematic over- or underestimation of the electron temperature can result in false correlations between the derived elemental abundances and mimic the effects of abundance variations which we are investigating. Although requiring a 7:1 S/N in [O III] λ4363 in order to determine T_e (§ 3.3) should guard against such pitfalls, we have constructed a set of element-element scatter plots to search for temperature biases as well as real correlations. We analyzed data from the four slit positions using the large (12″.5) extraction windows as in Figure 7, totaling 18 distinct locations. No significant spatial information is lost in this process since the physical parameters and abundances plotted in Figure 3 change slowly across

TABLE 4

POSITION C6 AND C20 LINE STRENGTHS

Line	Position C6 ($I_0/I_{H\beta}$)	Position C20 ($I_0/I_{H\beta}$)
3727 [O II]	2.557 ± 0.092	2.576 ± 0.104
3868 [Ne III].....	0.238 ± 0.012	0.303 ± 0.026
4068 [S II]	0.013 ± 0.003	<0.015 (3 σ)
4076 [S II]	0.006 ± 0.003	<0.015 (3 σ)
4101 Hδ	0.246 ± 0.008	0.090 ± 0.016
4340 Hγ	0.462 ± 0.011	0.387 ± 0.012
4363 [O III].....	0.024 ± 0.002	<0.025(3 σ)
4471 He I	0.041 ± 0.003	<0.020(3 σ)
4686 He II.....	0.014 ± 0.003	<0.007(3 σ)
4861 Hβ.....	1.000 ± 0.019	1.000 ± 0.020
4969 [O III].....	1.335 ± 0.025	1.053 ± 0.020
5007 [O III].....	4.036 ± 0.075	3.153 ± 0.059
5876 He I	0.117 ± 0.004	0.108 ± 0.005
6312 [S III]	0.017 ± 0.002	0.014 ± 0.001
6548 [N II]	0.065 ± 0.003	0.106 ± 0.006
6564 Hα.....	2.832 ± 0.122	2.836 ± 0.122
6584 [N II]	0.180 ± 0.008	0.229 ± 0.011
6678 He I	0.029 ± 0.002	0.023 ± 0.003
6717 [S II]	0.163 ± 0.008	0.222 ± 0.011
6731 [S II]	0.121 ± 0.006	0.160 ± 0.008
c(Hβ)	0.10 ± 0.04	0.14 ± 0.04
F(Hβ) ($\times 10^{14}$).....	4.3 ± 0.1	2.1 ± 0.0
EW(Hβ)	282 ± 5	11 ± 1
n_e (cm^{-3}).....	≤100.	≤100.

the slit, but the S/N is improved considerably over the small-aperture analyses. In all 18 apertures, the λ4363 line is strong enough to enable a *direct* measurement of T_e.

In Figure 8 we plot the N/O versus the O/H abundances for all 18 of these apertures using different symbols for each slit position. Locations along slits C and D corresponding to Knot 5, which has lower N/O and higher O/H than the rest of the galaxy, are distinguished with filled symbols. Filled inverted triangles define the correlation expected if systematic temperature errors were present in the data. A set of points with uniform abundances but significant temperature uncertainties would spread out along the direction of filled triangles. The filled triangle in the center of the diagram represents a hypothetical (but typical of NGC 4214) emission-line region with an oxygen abundance 12 + log (O/H) = 8.23, N/O = −1.28, and T_e = 10,000 K. The other solid triangles were derived by taking the same input emission-line strengths and artificially imposing different electron temperatures of 9000 and 11,000 K. One is labeled with an arrow indicating the temperature and direction of increasing temperature. The set of filled squares illustrates the effect of artificially perturbing the reddening parameter, c(Hβ), by 0.1. An arrow indicates the direction of increasing c(Hβ). A set of points with uniform abundances and temperature but significant uncertainties in c(Hβ) would spread out along the direction of filled squares. From Figure 8 it is evident that the derived oxygen abundance depends rather sensitively on T_e, while the N/O ratio is fairly insensitive to assumptions or uncertainties in T_e. This confirms that searching for N/O variations is a reasonably robust method of looking for abundance variations despite temperature uncertainties or possibly genuine T_e variations within the H II region.

Figure 8 illustrates the distinctly higher O/H abundance and lower N/O abundance present in the vicinity of Knot 5. The mean 12 + log (O/H) for the five data points from Knot 5 is 8.265 ± 0.014 compared to 8.170 ± 0.013 for the rest of the galaxy. The log (N/O) in Knot 5 is lower by the same 0.1 dex, −1.381 ± 0.030 compared to −1.273 ± 0.025 for the other 13 locations in rest of the galaxy. A best-fit line has a slope of −0.798 ± 0.350 and is steeper than the slope expected from systematic temperature errors (−0.30). The correlation coefficient of −0.721 indicates that such a distribution of 18 points selected from a random distribution would have an equal or greater degree of correlation less than one out of 1000 times. A formal linear fit to the points excluding the five points from Knot 5 shows only a weak correlation and a slope consistent with uniform abundances in the presence of small T_e uncertainties.

The O enhancement in Knot 5 is of the correct sense and magnitude to account for the N/O underabundance, and we conclude that N/H is constant throughout the galaxy. Figure 9 shows the N/H abundance versus O/H. The N/H abundance is consistent with a constant value at all locations (slope = 0.203 ± 0.379, linear correlation coefficient 0.45), which supports the O pollution interpretation for regions near Knot 5. A plot of log (S/O) versus log (O/H) in Figure 10 shows that S/O is consistent with a constant value. A formal fit yields a slope of 0.12 ± 0.13 with a correlation coefficient of 0.260. This lack of correlation is consistent with theoretical expectations and observations of low-metallicity systems that show that S and O occur in the same ratio. The value of log (S/O) ~ −1.6 is close to the solar value of −1.66 (Anders & Grevesse 1989) and supports the findings of Garnett (1989) that the S/O ratio is close to solar for all low-metallicity H II regions.

In Figure 11 we present a plot similar to that of Figure 8 showing He/H versus the O/H. The five locations in Knot 5 at the upper end of the O/H range differ only marginally in their helium abundances. The mean He/H of the locations in Knot 5 is 0.0862 ± 0.0019 compared to 0.0842 ± 0.0019 for the rest of the galaxy. Solid inverted triangles are again used in to mark the trend resulting from simulated temperature excursions on either side of T = 10,000 K for a point with He/H = 0.085 (no correction is made for collisional excitation of He I λ5876). The observed slope in the data, 0.0357 ± 0.0350, is inconsistent with that expected if large temperature uncertainties dominated affected the trend (slope = −0.0152).

Figure 12 demonstrates the observed relation between the Ne/O ratio and O/H. The mean Ne/O for the data from Knot 5 is 0.152 ± 0.008 compared to 0.182 ± 0.008 for the rest of the galaxy. A linear fit to the data has a slope of −0.375 ± 0.152 with a linear correlation coefficient of −0.37. This correlation, if genuine, is surprising since both Ne and O are thought to be produced together and should always appear in the same ratio. O pollution without accompanying Ne pollution would be a challenge to explain theoretically. The dependence of Ne/O on temperature is very weak, so T_e uncertainties are unlikely to affect the measurements significantly. A more probable explanation may be that equation (15) is not strictly true. To check this, we consulted the photoionization models of Stasińska (1990). The models for metallicities of 20% of the solar value (her series "D") showed that the ionization fractions of O^{++} and Ne^{++} are not always equal. Specifically, for low-ionization parameters, the Ne^{++}/Ne fraction is usually higher than the O^{++}/O fraction by 10%–20%. At high values of the ionization parameter, the two ionization fractions are nearly equal. Thus, if the calculated abundance differences are due to the inadequacy of equation (15), one would expect a trend of increasing Ne/O with decreasing

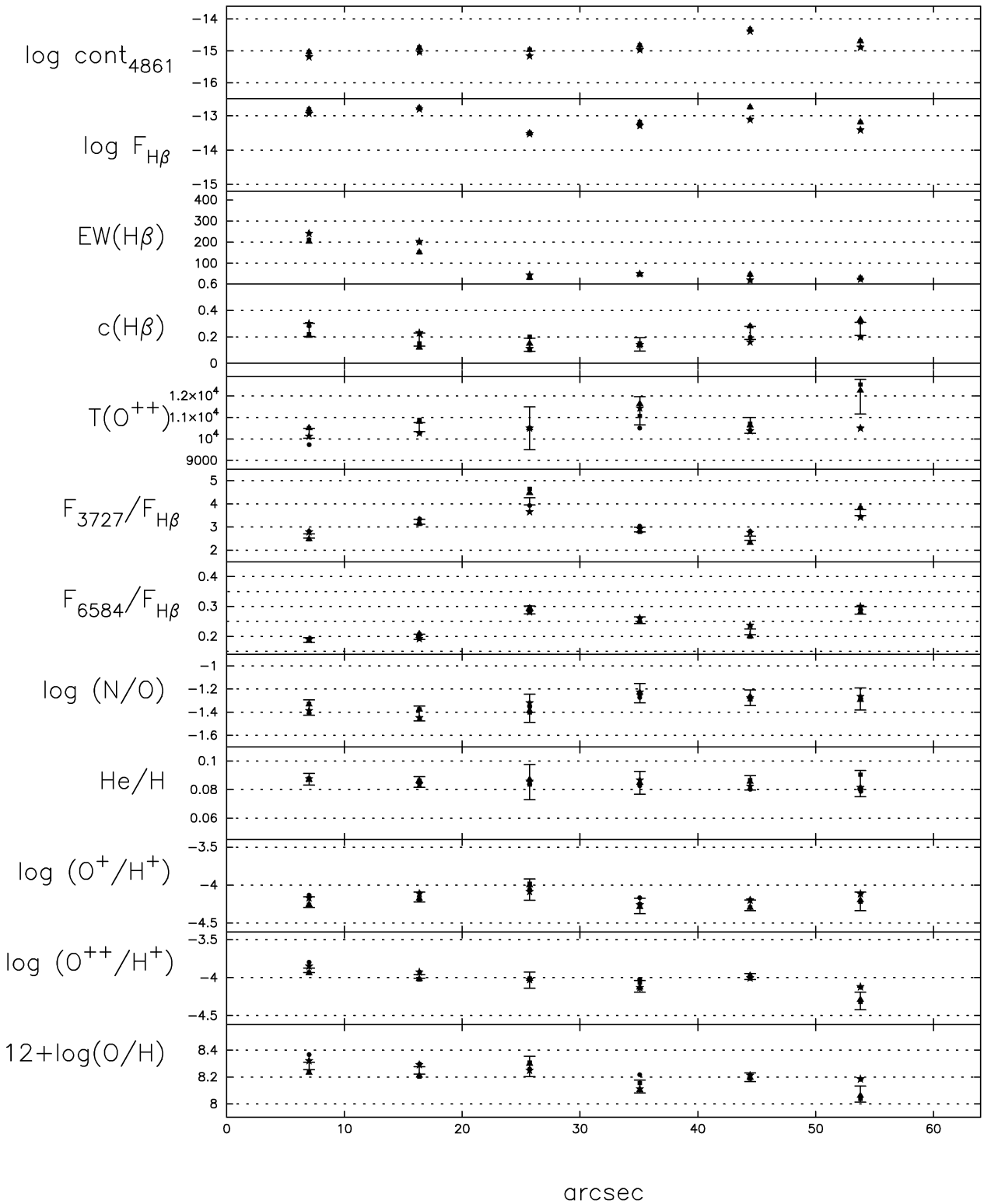

FIG. 7.—Same as Fig. 3*c* but with 4 times larger extraction apertures. The correspondence with the smaller apertures in Fig. 3*c* is good, and the differences in O/H and N/O between Knot 1 and Knot 5 are more clearly visible.

ionization parameter (or increasing O^+/O^{++}). In Figure 13 we plot the Ne/O abundance versus the fraction of single to doubly ionized oxygen (O^+/O^{++}). The points from Knot 5 are again discernible as a group. The slope of 0.037 ± 0.031 is positive, in accordance with calculated Ne/O variations due to ionization parameter variations. The linear correlation coefficient of 0.39 indicates such a correlation of this or higher significance would be observed one out of 10 times in a random sample.

In summary, the above figures illustrate that temperature uncertainties are not a factor in the data and that the regions near Knot 5 have clearly elevated O/H abundances,

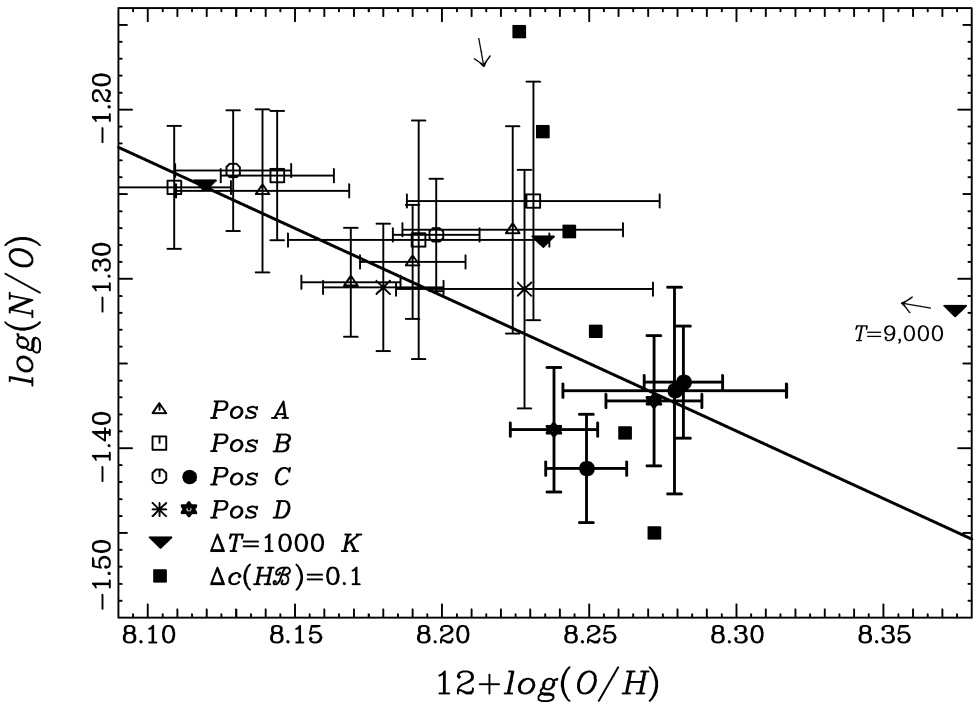

FIG. 8.—O/H vs. N/O abundances at 18 positions in NGC 4214 using wide (12.″5) apertures. Solid circles and stars denote regions near Knot 5 that show higher O/H abundances and lower N/O ratios (0.1 dex) than the rest of the surveyed region. Filled triangles/squares illustrate effect on the derived abundances when the adopted $T_e/c(H\beta)$ is artificially displaced by 1000 K/0.1. The solid line is a least-squares fit treating O/H as the independent variable.

lower N/O ratios, but similar He/H and Ne/O ratios relative to the rest of the galaxy. The only abundance fluctuations observed appear to be due to O pollution in the vicinity of Knot 5.

4.4. *Comparison of Regions with Wolf-Rayet Stars*

To investigate directly the possibility that evolved massive stars, specifically Wolf-Rayet stars, pollute the local ISM with recent nucleosynthesis products (Pagel et al. 1986; Kunth & Sargent 1986), we have constructed histograms comparing the O, N/O, and He abundances in regions with observed W-R features to those regions with no signs of W-R stars. Figure 14 shows, in histogram form, the mean N/O, He/H, and O/H abundance for 82 distinct spatial locations from Figure 3. Dashed lines denote those regions with either clear signs of W-R stars or possible

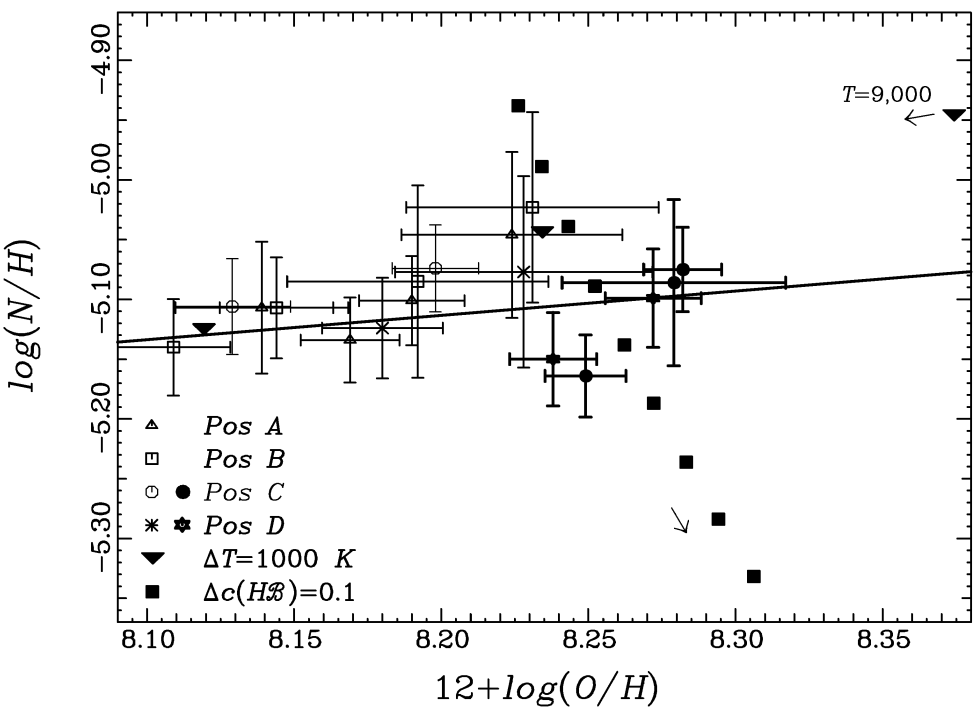

FIG. 9.—Value of log (N/H) vs. 12 + log (O/H) similar to Fig. 8. N/H is constant at all samples locations consistent with an O enrichment hypothesis.

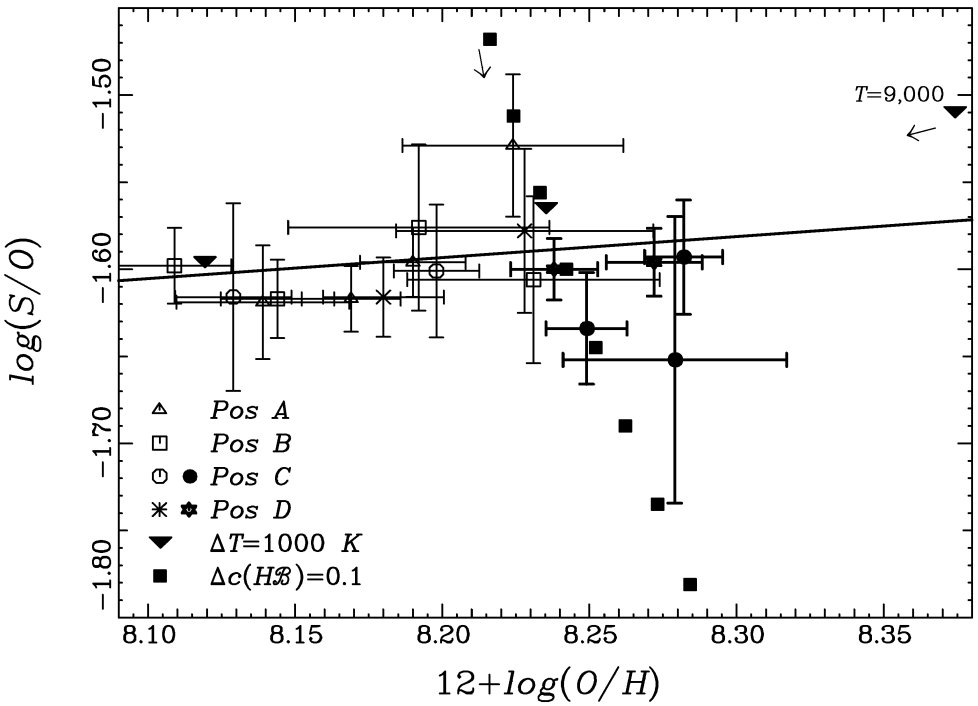

FIG. 10.—Value of log (S/O) vs. 12 + log (O/H). S/O is constant at all samples locations, consistent with theoretical expectations and observations that show that S and O are produced in the same ratio.

broad emission in the vicinity of λ4686. Solid histograms are used for regions with no signs of W-R stars. The mean and error-of-the-mean is indicated with symbols and error bars. Neither the N/O nor the He/H distributions show any appreciable difference between the regions with and without W-R features. There is a small but statistically significant (2 σ) difference in the O abundance between the two samples. The mean of the regions with W-R features is 8.208 ± 0.010 compared to 8.232 ± 0.006 for the regions without. Upon closer examination, we find this difference is due to a small

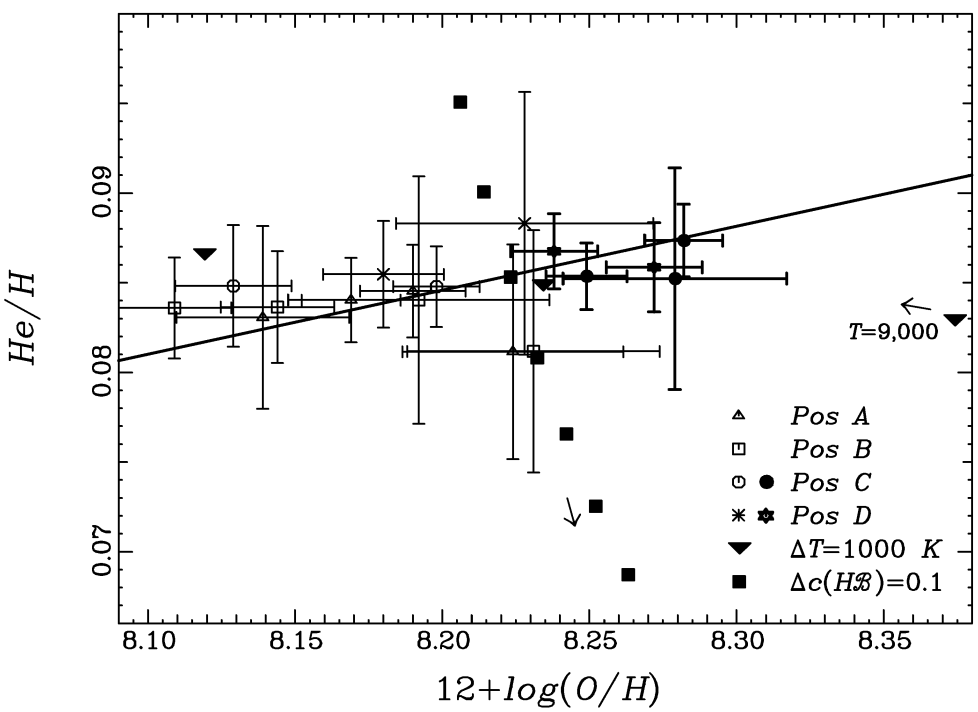

FIG. 11.—He/H vs. O/H abundances at 18 positions in NGC 4214 using wide (12.″5) apertures. Solid circles and stars denote regions near Knot 5. Annotations are same as Fig. 8.

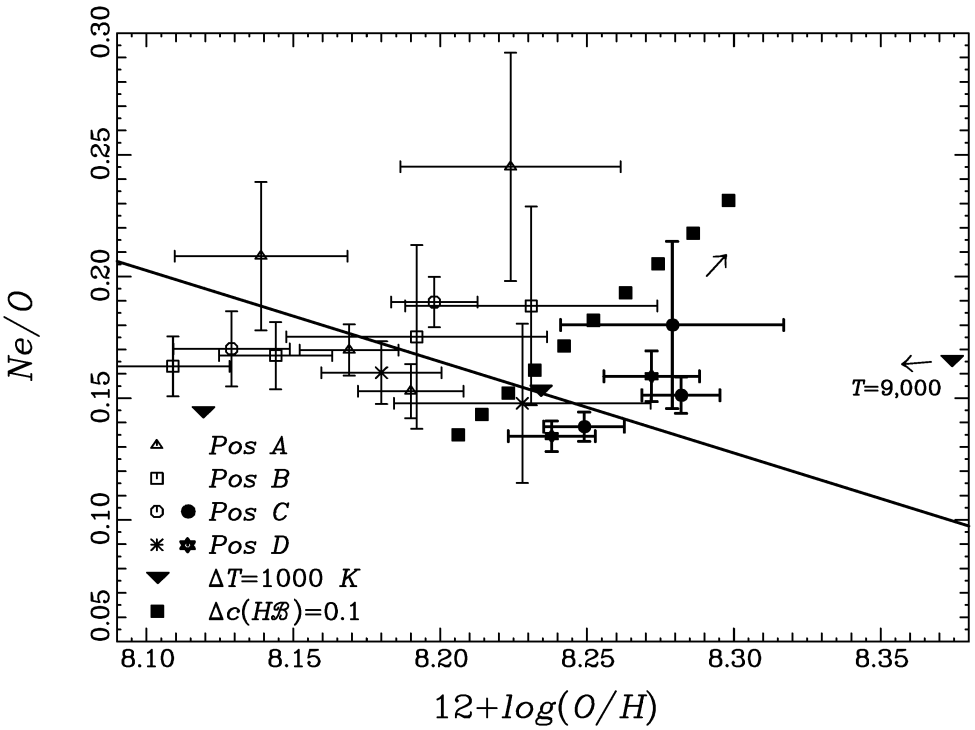

FIG. 12.—Ne/O ratio vs. O/H. Solid circles and stars denote regions near Knot 5. Annotations are same as Fig. 8.

bias introduced by assuming $T_e = 10{,}500$ K for regions without strong λ4363 emission. Regions where constant T_e has been adopted have a higher mean oxygen abundance than regions with direct T_e measurements, which suggests that the adopted T_e is too low. Since regions without W-R stars are typically regions with lower nebular surface brightness that have S/N(λ4363) below our chosen threshold, regions lacking W-R stars erroneously appear in Figure 14

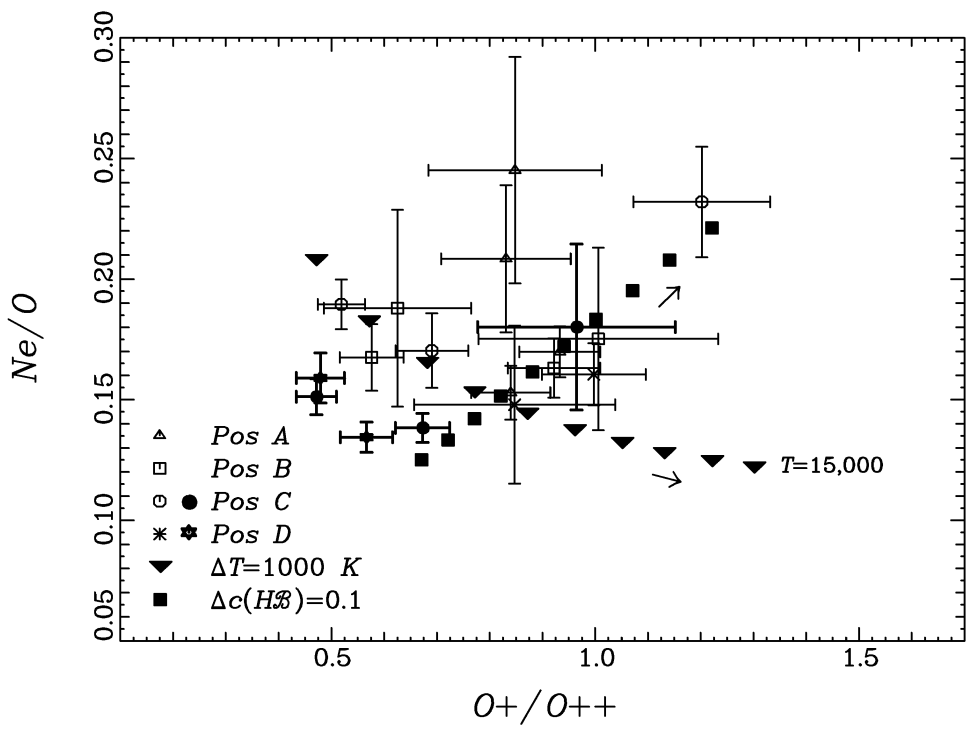

FIG. 13.—Ne/O ratio vs. the ratio of singly to doubly ionized oxygen (O^{++}/O^{+}). The correlation is weak and is roughly consistent with ionization effects being responsible for the observed weak correlation between Ne/O and O/H.

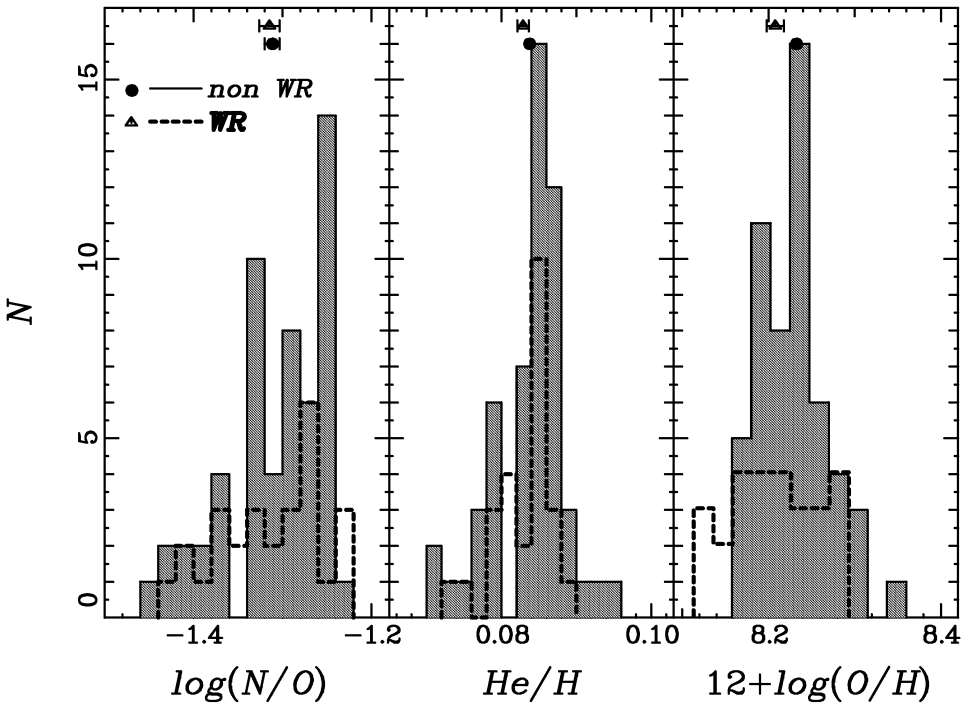

FIG. 14.—Histogram of log (N/O), He/H, and 12 + log (O/H) abundances derived from 82 spatial locations using the small (3″.1) extraction apertures. Data represent the weighted mean of all data at a given spatial location from different nights. Spectra with strong or possible broad emission from Wolf-Rayet stars are distinguished from those locations lacking evidence for W-R stars. There is no systematic difference between the two samples seen in N/O or He/H. The mean oxygen abundance in regions with W-R stars is 2 σ lower than regions lacking W-R stars, but this small difference is due to bias as explained in the text.

to have systematically higher O abundances than the W-R regions. N/O and He/H abundances are not affected by this bias since they are much less sensitive to T_e uncertainties. The O abundance differences between Knot 5 and the rest of the galaxy are also *not* affected by this bias since direct T_e determinations are possible for the wide aperture spectra used to derive abundances in Figures 8, 9, 10, 11, 12, and 13.

5. DISCUSSION

Although we find no evidence that winds from O or W-R stars have polluted their local environment with N and/or He on short timescales in NGC 4214, we do find a region consistent with O pollution from supernovae. There also remains the suspicion that short-term chemical enrichment (self-pollution) of H II regions does occur in some low-metallicity emission line galaxies, which makes them unsuitable for use in primordial abundance and galactic chemical evolution work (Kunth & Sargent 1986; Pagel et al. 1992; Esteban & Peimbert 1995). Helium is usually the element of interest such studies, but He fluctuations will be hard to detect against a background of preexisting primordial helium. If W-R winds and massive stars, in which N and He are both plentiful, are a source of enrichment, N seems the best surrogate for He, and searches for N enrichment should prove most helpful. In fact, Pagel et al. (1992) found a significantly higher correlation between He and N than between He and O. While the absence of localized enrichments in NGC 4214 may suggest that pollution effects are not serious, the relatively high metallicity of NGC 4214 compared to metal-poor galaxies commonly used in primordial abundance studies will necessarily mean that any local enrichment will be less pronounced; i.e., a given starburst's nucleosynthetic products will make a much smaller differential change in the nebular abundance of an already metal-rich medium. Future studies of a similar type should focus on spatially resolved studies of more metal-poor systems.

The possibility of localized O pollution is not without precedent. Cunha & Lambert (1994) find a subgroup of the youngest O and B stars in the Orion Nebula that are colocated on the sky and exhibit 40% higher O and Si abundances than three other subgroups. They suggest these stars were formed in a region already polluted by the O-rich ejecta of Type II supernova events.

Here, we will be content to estimate crudely the magnitude of the apparent O enrichment in Knot 5. If we take the size of the enriched region to be a sphere 5″ (103 pc) in radius and assume a density of 100 atoms cm^{-3} and a filling factor of 0.01 which is typical of H II regions (calculated from the tabulated $F(\mathrm{H}\beta)$ for slit position C6, the adopted distance and projected slit dimensions), then $\sim 30\ M_\odot$ of O are required to raise the O abundance of the ISM by 0.1 dex above the rest of the galaxy. This is roughly the equivalent O yield of five 40 $M_\odot$ stars (Maeder 1992). O-enriched supernovae traveling at an average speed of 100 km s^{-1} would require 1 Myr to envelop a region the size of Knot 5. Whether such material would cool and become well mixed with the surrounding ISM on such timescales is an open question that deserves further treatment but is beyond the scope of this work (see Tenorio-Tagle 1996).

In future comparisons of abundance enrichment models to observations, geometrical dilution effects should be considered since the visibility of abundance enrichments must depend on how well the spectroscopic slit and extraction aperture are matched to spatial scale of the enrichment. It may be easy to miss pockets of enrichment in nearby

systems. In more distant galaxies, the signature of pollution may get diluted by emission from the unenriched portions of the H II region(s).

The lack of any localized enrichment associated with massive stars in NGC 4214 elevates the significance of NGC 5253 and its N-overabundant region. In NGC 5253, the region mapped by Walsh & Roy (1989) and investigated by others (Pagel et al. 1992) clearly shows a 60 pc diameter region in which N is overabundant by a factor of 2 compared to the rest of the galaxy. This region is coincident with W-R features, and there is no accompanying increase in any other elements with the possible exception of He reported to be elevated by Campbell et al. (1986) but not by Walsh & Roy (1989). The high N/O ratio does not appear to be explainable in terms of shocks or unusual excitation mechanisms. A combination of enrichment from W-R winds (Walsh & Roy 1989) and unusual gas kinematics that could affect the dispersal and mixing of fresh nucleosynthesis products may be at work.

We will conclude here with a quantitative attempt to estimate from published data the likelihood that galaxies with W-R stars are affected by abundance pollution. We have collected from the literature a large representative sample of spectroscopic measurements in metal-poor galaxies ($12 + \log \mathrm{O/H} < \sim 8.4$) and have recomputed the O, N/O, and He/H abundances in a self-consistent manner using the program described in § 3. The details of the selection process and analysis are described in the Appendix, and abundances are tabulated in Table 5.

Figure 15 displays the O/H and N/O abundances for 72 measurements in 60 galaxies reported in Table 5. Multiple measurements showing different abundances within a single galaxy are plotted separately connected by dotted lines. Filled circles distinguish galaxies with reported W-R features from those without signs of W-R stars (*open circles*). A heavy vector shows the theoretical evolution of metal-poor galaxies during an early phase in the starburst process when massive stars are contributing to O production and pollution (Garnett 1990, Fig. 7). While it may not be possible to verify observationally that an *ensemble* of H II galaxies evolve in the prescribed manner, it is interesting to compare abundance measurements at multiple locations in *individual* nearby galaxies to the expected variations. The slope of the O-pollution vector is strikingly similar to that of the dotted lines connecting multiple measurements in NGC 5253, NGC 4214, and NGC 3125, consistent with the hypothesis that we are witnessing ongoing O pollution in these systems. If this is the case, then it is important to identify the mechanism by which enriched stellar winds and supernovae ejecta cool and mix with the surrounding ISM on timescales comparable to that of the star formation episodes.

The weighted mean log (N/O) for a subsample of 22 objects in Figure 15 with W-R features is -1.36 ± 0.02 compared to -1.45 ± 0.01 for a subsample of 50 objects without W-R features. The difference between the two subsamples is significant at the 4 σ level, giving a <0.001 probability that the means are coincident. If NGC 5253 (which is heavily represented with seven data points distributed over a wide range in N/O and O/H) is neglected, the means become -1.41 ± 0.02 for the 20 measurements with W-R features versus -1.46 ± 0.01 for 45 measurements without W-R features. In this latter case, the difference between the two subsamples is still significant at the 2 σ level, which gives a 0.04 probability that the means are coincident. In Figure 15, triangles near 12 + log (O/H) mark the weighted mean and uncertainty of the two subsamples when NGC 5253 is excluded. It appears that there is a significant difference between the two subsamples, but the statistics are

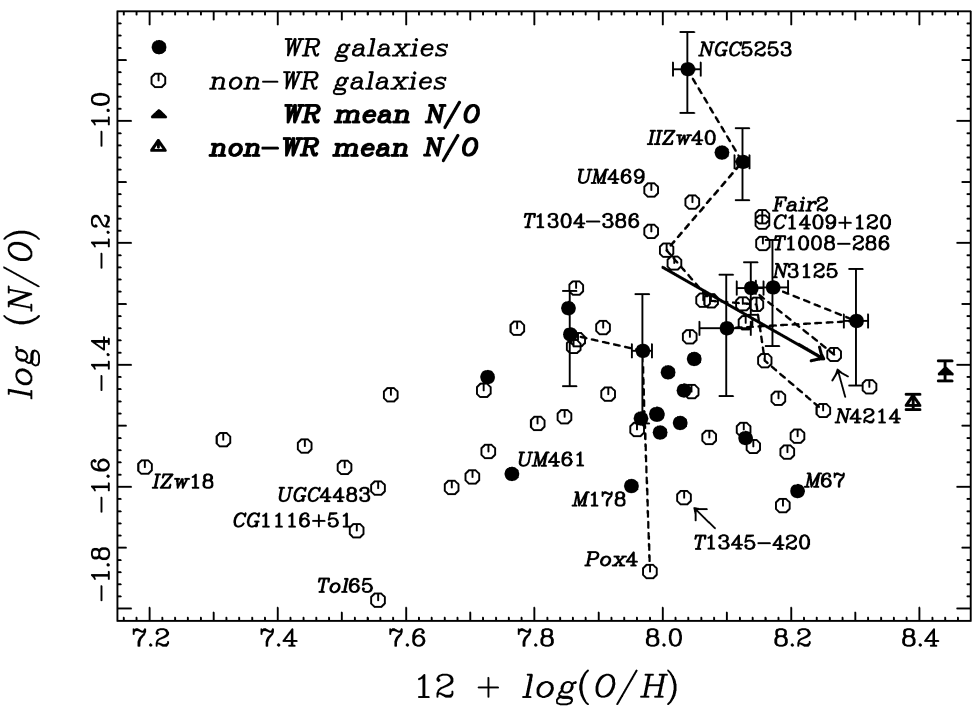

FIG. 15.—Value of log (N/O) vs. 12 + log (O/H) for 72 measurements of 60 low-metallicity galaxies from the literature. Abundances have been recomputed in a self-consistent manner from published line strengths. Triangles mark the average values of log (N/O) for galaxies with and without W-R features when NGC 5253 is removed from the sample. The difference between the two subsamples becomes negligible if galaxies with 12 + log (O/H) < 7.6 are excluded from the sample. A heavy vector shows the theoretical evolution of metal-poor galaxies during a period of oxygen pollution (Garnett 1990, Fig. 7).

TABLE 5

RECOMPUTED AND TABULATED ABUNDANCES

Galaxy	$T(O^{++})$	12 + log (O/H)	log (N/O)	He/H	W-R	References
I Zw 18	18870 ± 690	$7.193^{+0.022}_{-0.024}$	$-1.568^{+0.055}_{-0.066}$	0.077 ± 0.004	N	1
I Zw 18nw[a]	19400 ± 790	$7.175^{+0.024}_{-0.026}$	$-1.552^{+0.065}_{-0.076}$	0.077 ± 0.005[g]	N	1
I Zw 18se[a]	17060 ± 1460	$7.279^{+0.050}_{-0.057}$	$-1.615^{+0.103}_{-0.135}$	0.077 ± 0.009[g]	N	1
0940+544N[b]	21650 ± 560	$7.315^{+0.016}_{-0.016}$	$-1.523^{+0.068}_{-0.081}$	0.093 ± 0.005	N	2
1159+545[b]	19320 ± 550	$7.442^{+0.018}_{-0.019}$	$-1.533^{+0.062}_{-0.072}$	0.086 ± 0.005	N	2
1415+437[b]	18210 ± 260	$7.504^{+0.014}_{-0.014}$	$-1.568^{+0.042}_{-0.047}$	0.092 ± 0.003	N	3
UGC 4483	16530 ± 260	$7.556^{+0.014}_{-0.015}$	$-1.602^{+0.044}_{-0.050}$	0.082 ± 0.004	N	
0832+699[b]	16560 ± 270	$7.553^{+0.015}_{-0.016}$	$-1.629^{+0.053}_{-0.060}$	0.082 ± 0.004	N	2
UGC 4483s[a]	16270 ± 850	$7.571^{+0.035}_{-0.039}$	$-1.542^{+0.077}_{-0.093}$	0.082 ± 0.007	N	4
Tol 65[c]	17480 ± 870	$7.556^{+0.032}_{-0.035}$	$-1.786^{+0.151}_{-0.233}$	0.070 ± 0.010	N	5
CG 1116+51	16680 ± 1100	$7.523^{+0.042}_{-0.046}$	$-1.672^{+0.099}_{-0.128}$	0.078 ± 0.009	N	6
T1214−277[a]	18760 ± 750	$7.576^{+0.025}_{-0.026}$	$-1.449^{+0.080}_{-0.098}$	0.081 ± 0.008	N	7
1211+540[b]	17110 ± 240	$7.671^{+0.010}_{-0.011}$	$-1.601^{+0.058}_{-0.067}$	0.083 ± 0.007[g]	N	2
1249+493[b]	16630 ± 580	$7.703^{+0.024}_{-0.025}$	$-1.584^{+0.082}_{-0.101}$	0.088 ± 0.007	N	3
T1304−353[c]	18290 ± 810	$7.721^{+0.033}_{-0.036}$	$-1.442^{+0.127}_{-0.181}$	0.078 ± 0.009	N	8
Pox 186[b]	17190 ± 380	$7.726^{+0.015}_{-0.016}$	$-1.420^{+0.198}_{-0.373}$	0.085 ± 0.008	Y	5
1420+554[b]	17700 ± 360	$7.728^{+0.014}_{-0.014}$	$-1.542^{+0.078}_{-0.096}$	0.092 ± 0.005	N	2
UM 461[a]	17020 ± 440	$7.764^{+0.019}_{-0.020}$	$-1.579^{+0.059}_{-0.068}$	0.084 ± 0.005[g]	Y	7
C1543+091[c]	16290 ± 580	$7.773^{+0.025}_{-0.027}$	$-1.340^{+0.115}_{-0.156}$	0.084 ± 0.007	N	8
1331+493	15780 ± 200	$7.805^{+0.011}_{-0.011}$	$-1.496^{+0.044}_{-0.050}$	0.091 ± 0.003	N	
1331+493N[b]	15910 ± 210	$7.801^{+0.011}_{-0.011}$	$-1.492^{+0.050}_{-0.056}$	0.090 ± 0.003	N	2
1331+493S[b]	13530 ± 870	$7.893^{+0.047}_{-0.053}$	$-1.495^{+0.089}_{-0.112}$	0.104 ± 0.011	N	3
Mrk 36	14950 ± 410	$7.847^{+0.021}_{-0.022}$	$-1.485^{+0.089}_{-0.125}$	0.092 ± 0.009	N	
Mrk 36[c]	14900 ± 420	$7.847^{+0.022}_{-0.023}$	$-1.459^{+0.108}_{-0.144}$	0.092 ± 0.010	N	8
Mrk 36[d]	15410 ± 1930	$7.854^{+0.081}_{-0.099}$	$-1.559^{+0.159}_{-0.254}$	0.086 ± 0.027	N	9, 10
Pox 120[c]	15870 ± 410	$7.852^{+0.019}_{-0.020}$	$-1.307^{+0.088}_{-0.110}$	0.082 ± 0.007	Y	5
Pox 4:						
C1148−203[c]	14980 ± 410	$7.855^{+0.023}_{-0.025}$	$-1.350^{+0.071}_{-0.085}$	0.081 ± 0.006	Y	8
Pox 4[c]	14620 ± 280	$7.968^{+0.015}_{-0.016}$	$-1.377^{+0.093}_{-0.119}$	0.080 ± 0.005	Y	5
Pox 4NW[c]	13560 ± 320	$7.980^{+0.028}_{-0.030}$	$-1.739^{+0.081}_{-0.099}$	0.065 ± 0.006	N	5
Pox 108[c]	15430 ± 330	$7.861^{+0.018}_{-0.019}$	$-1.370^{+0.080}_{-0.099}$	0.076 ± 0.007	N	5
1152+579[b]	15560 ± 190	$7.865^{+0.010}_{-0.010}$	$-1.274^{+0.047}_{-0.052}$	0.107 ± 0.004	N	2
Pox 105[c]	15300 ± 330	$7.868^{+0.018}_{-0.019}$	$-1.359^{+0.081}_{-0.099}$	0.074 ± 0.007	N	5
Fairall 30[c]	14550 ± 310	$7.907^{+0.020}_{-0.021}$	$-1.339^{+0.064}_{-0.076}$	0.085 ± 0.011[g]	N	8
C0840+120[c]	14140 ± 420	$7.915^{+0.025}_{-0.027}$	$-1.448^{+0.078}_{-0.095}$	0.089 ± 0.006	N	8
Mrk 178	14610 ± 390	$7.950^{+0.020}_{-0.021}$	$-1.599^{+0.061}_{-0.071}$	0.089 ± 0.005	Y	6
UM 462[c]	14200 ± 240	$7.960^{+0.017}_{-0.018}$	$-1.506^{+0.080}_{-0.098}$	0.092 ± 0.011	N	8
1437+370[b]	14020 ± 220	$7.965^{+0.014}_{-0.014}$	$-1.488^{+0.053}_{-0.060}$	0.088 ± 0.003	Y	2
T1304−386[c]	14040 ± 350	$7.982^{+0.020}_{-0.021}$	$-1.181^{+0.070}_{-0.084}$	0.095 ± 0.007	N	8
UM 469[c]	12800 ± 1260	$7.982^{+0.068}_{-0.080}$	$-1.113^{+0.125}_{-0.177}$	0.090 ± 0.017	N	8
Pox139[c]	14000 ± 310	$7.990^{+0.020}_{-0.021}$	$-1.482^{+0.082}_{-0.101}$	0.082 ± 0.006	Y	5
Mrk 600[a]	14280 ± 550	$7.991^{+0.028}_{-0.030}$	$-1.481^{+0.125}_{-0.176}$	0.085 ± 0.013	N	7
Tol 2[c]	13220 ± 230	$7.995^{+0.024}_{-0.025}$	$-1.511^{+0.084}_{-0.105}$	0.066 ± 0.006	N	5
NGC 5253:						
N5253A[c]	12750 ± 250	$8.006^{+0.021}_{-0.022}$	$-0.915^{+0.061}_{-0.072}$	0.119 ± 0.006	Y	8
N5253B[c]	10910 ± 1240	$8.250^{+0.084}_{-0.104}$	$-1.475^{+0.138}_{-0.203}$	0.089 ± 0.018	N	8
N5253-1[e]	12010 ± 100	$8.124^{+0.011}_{-0.012}$	$-1.067^{+0.055}_{-0.063}$	0.079 ± 0.003	Y	11
N5253-2[e]	11340 ± 770	$8.146^{+0.054}_{-0.062}$	$-1.301^{+0.096}_{-0.124}$	0.082 ± 0.009	N	11
N5253-4[e]	11990 ± 730	$8.159^{+0.047}_{-0.053}$	$-1.393^{+0.090}_{-0.114}$	0.074 ± 0.009	N	11
N5253-5[e]	12220 ± 540	$8.075^{+0.037}_{-0.041}$	$-1.295^{+0.075}_{-0.091}$	0.080 ± 0.007	N	11
N5253-6[e]	12570 ± 620	$8.006^{+0.041}_{-0.045}$	$-1.212^{+0.078}_{-0.096}$	0.086 ± 0.004	N	11
1135+581[b]	13020 ± 160	$8.007^{+0.013}_{-0.013}$	$-1.412^{+0.051}_{-0.058}$	0.086 ± 0.004[g]	Y	2
I Zw 123[d]	14370 ± 1600	$8.018^{+0.081}_{-0.099}$	$-1.233^{+0.138}_{-0.204}$	0.084 ± 0.004	N	9, 10
0946+558[b]	13400 ± 210	$8.026^{+0.015}_{-0.015}$	$-1.495^{+0.052}_{-0.059}$	0.090 ± 0.003	Y	2
0948+532[b]	13360 ± 210	$8.032^{+0.015}_{-0.015}$	$-1.442^{+0.053}_{-0.061}$	0.090 ± 0.004	Y	2
T1345−420[c]	13320 ± 670	$8.033^{+0.038}_{-0.041}$	$-1.618^{+0.091}_{-0.116}$	0.120 ± 0.021[g]	N	8
1533+469[b]	14050 ± 480	$8.042^{+0.027}_{-0.029}$	$-1.354^{+0.064}_{-0.075}$	0.110 ± 0.008	N	3

TABLE 5—*Continued*

Galaxy	$T(O^{++})$	12 + log (O/H)	log (N/O)	He/H	W-R	References
II Zw 40	13350 ± 210	$8.091^{+0.013}_{-0.014}$	$-1.052^{+0.059}_{-0.077}$	0.093 ± 0.013[g]	Y[h]	
II Zw 40[c]	13470 ± 360	$8.046^{+0.025}_{-0.026}$	$-1.042^{+0.095}_{-0.121}$	0.094 ± 0.016[g]	N	8
II Zw 40[c]	13370 ± 250	$8.106^{+0.016}_{-0.017}$	$-1.184^{+0.083}_{-0.103}$	0.094 ± 0.027[g]	Y	5
II Zw 40[d]	12210 ± 950	$8.234^{+0.075}_{-0.091}$	$-1.104^{+0.193}_{-0.357}$	0.077 ± 0.057[g]	N	9, 10
UM 439[c]	14100 ± 340	$8.045^{+0.020}_{-0.020}$	$-1.444^{+0.090}_{-0.114}$	0.072 ± 0.011[g]	Y	7
T0645−376[c]	12770 ± 1590	$8.046^{+0.083}_{-0.102}$	$-1.133^{+0.148}_{-0.226}$	0.077 ± 0.020	N	8
II Zw 70[d]	12220 ± 1160	$8.063^{+0.075}_{-0.090}$	$-1.294^{+0.125}_{-0.177}$	0.105 ± 0.035[g]	N	9, 10
T1334−396[c]	13590 ± 460	$8.072^{+0.030}_{-0.032}$	$-1.519^{+0.114}_{-0.155}$	0.092 ± 0.011	N	8
NGC 4861	12900 ± 1400	$8.075^{+0.019}_{-0.020}$	$-1.377^{+0.059}_{-0.068}$	0.083 ± 0.004	Y	6
NGC 3125:						
T1004−296SE[c]	11820 ± 540	$8.099^{+0.038}_{-0.042}$	$-1.340^{+0.088}_{-0.111}$	0.130 ± 0.025[g]	Y	8
T1004−296NW[c]	11040 ± 240	$8.171^{+0.024}_{-0.026}$	$-1.273^{+0.078}_{-0.096}$	0.129 ± 0.016[g]	Y	8
Tol 3[c]	10960 ± 200	$8.301^{+0.019}_{-0.019}$	$-1.328^{+0.085}_{-0.106}$	0.104 ± 0.015[g]	Y	5
Tol 35	12270 ± 210	$8.128^{+0.017}_{-0.018}$	$-1.520^{+0.058}_{-0.071}$	0.087 ± 0.007	?[h]	
Tol 35[c]	12660 ± 320	$8.104^{+0.024}_{-0.025}$	$-1.521^{+0.080}_{-0.098}$	0.074 ± 0.015[g]	Y	5
T1324−276[c]	11980 ± 280	$8.150^{+0.023}_{-0.025}$	$-1.369^{+0.083}_{-0.102}$	0.091 ± 0.008	N	8
0633−415	12650 ± 460	$8.127^{+0.029}_{-0.031}$	$-1.319^{+0.060}_{-0.070}$	0.089 ± 0.006	?	
T0633−415[c]	12660 ± 660	$8.125^{+0.041}_{-0.045}$	$-1.300^{+0.095}_{-0.122}$	0.088 ± 0.010	N	8
0633−415[a]	12650 ± 650	$8.129^{+0.040}_{-0.044}$	$-1.331^{+0.078}_{-0.095}$	0.090 ± 0.007	Y	7
LMC II2[a]	11650 ± 550	$8.126^{+0.050}_{-0.056}$	$-1.506^{+0.112}_{-0.151}$	0.103 ± 0.012	Y	12
Pox 36[c]	11970 ± 280	$8.141^{+0.029}_{-0.031}$	$-1.534^{+0.082}_{-0.101}$	0.109 ± 0.037[g]	N	7
C1409+120[c]	12660 ± 570	$8.155^{+0.035}_{-0.038}$	$-1.166^{+0.122}_{-0.171}$	0.117 ± 0.012	N	8
Fairall 2[c]	11770 ± 850	$8.155^{+0.055}_{-0.063}$	$-1.157^{+0.120}_{-0.166}$	0.081 ± 0.019	N	8
T1008−286[c]	13220 ± 460	$8.156^{+0.028}_{-0.030}$	$-1.201^{+0.098}_{-0.127}$	0.117 ± 0.013	N	8
T1457−262	11620 ± 360	$8.180^{+0.027}_{-0.030}$	$-1.455^{+0.069}_{-0.090}$	0.086 ± 0.006	N	
T1457−262A[c]	11690 ± 430	$8.159^{+0.033}_{-0.036}$	$-1.361^{+0.095}_{-0.122}$	0.098 ± 0.009	N	8
T1457−262B[c]	11450 ± 680	$8.222^{+0.047}_{-0.053}$	$-1.567^{+0.101}_{-0.133}$	0.077 ± 0.008	N	8
N6822-HuX[a]	11350 ± 1040	$8.187^{+0.072}_{-0.086}$	$-1.631^{+0.130}_{-0.187}$	0.067 ± 0.012	N	13
T0440−381[c]	11430 ± 540	$8.194^{+0.039}_{-0.043}$	$-1.543^{+0.089}_{-0.112}$	0.090 ± 0.008	N	8
Mrk 67[d]	11930 ± 1080	$8.209^{+0.077}_{-0.094}$	$-1.607^{+0.139}_{-0.206}$	0.083 ± 0.027	Y	9, 10
NGC 4214:						
N4214-K1–4[f]	10800 ± 340	$8.173^{+0.020}_{-0.022}$	$-1.274^{+0.042}_{-0.044}$	0.084 ± 0.003	Y	14
N4214-K5[f]	10550 ± 210	$8.267^{+0.015}_{-0.017}$	$-1.383^{+0.049}_{-0.052}$	0.078 ± 0.002	N?	14
Mrk 5[d]	11020 ± 970	$8.210^{+0.074}_{-0.090}$	$-1.517^{+0.659}_{-0.800}$	0.096 ± 0.030	N	9, 10
T1116−325[c]	10140 ± 630	$8.322^{+0.062}_{-0.073}$	$-1.436^{+0.119}_{-0.165}$	0.089 ± 0.015	N	8

[a] Abundances are computed from published dereddened line strengths and errors. We adopt the published $c(H\beta)$ but solve for T_e.

[b] We solve for $c(H\beta)$ from the published raw line fluxes. Uncertainties on $c(H\beta)$ are not given, so we adopt an intrinsic uncertainty of $\delta c(H\beta) = 0.04$.

[c] We solve for $c(H\beta)$ and T_e from the published raw line fluxes. Second-order contamination is present at the red end of the spectrum, so solutions for $c(H\beta)$ do not make use of $H\alpha$, as noted in original publications.

[d] We solve for $c(H\beta)$ and T_e from the published raw line fluxes. We use the lines redward of 6400 Å from Garnett 1990 in combination with the lines blueward of 6400 Å from French 1980.

[e] We start from the published dereddened line strengths. Listed errors on line strengths are inexplicably less than the uncertainty due to $c(H\beta)$ alone. We assume that $c(H\beta)$ errors were simply neglected, and we add in quadrature to the stated errors a contribution due to the published $\delta c(H\beta)$ before computing abundances.

[f] We solve for $c(H\beta)$ and T_e from the published raw line fluxes.

[g] He abundance computed from He I λ6678 due to possible galactic Na I absorption affecting the He I λ5876 emission line at this redshift.

[h] There are conflicting reports about the W-R content (see Walsh & Roy 1993).

REFERENCES.—(1) Skillman & Kennicutt 1993; (2) Izotov, Thuan, & Lipovetsky 1994; (3) Thuan, Izotov, & Lipovetsky 1995; (4) Skillman et al. 1994; (5) Kunth & Joubert 1985; (6) Kobulnicky & Skillman 1996; (7) Pagel et al. 1992; (8) Campbell, Terlevich, & Melnick 1986; (9) Garnett 1990; (10) French 1980; (11) Walsh & Roy 1989; (12) Mathis, Chu, & Peterson 1985; (13) Pagel, Edmunds, & Smith 1980; (14) this work.

heavily influenced by just a few measurements at the upper end of the N/O range, namely NGC 5253 and II Zw 40. II Zw 40 lies at low Galactic latitude and suffers considerable extinction, which makes making measurements of N/O more uncertain. There is also disagreement about whether W-R stars are detected or not (see Walsh & Roy 1993). Removing II Zw 40 from the sample further diminishes the differences between the two subsamples.

The most significant effect that gives rise to the apparent statistical difference between the W-R and non–W-R subsamples is the inclusion of galaxies at very low metallicity [12 + log (O/H) < 7.6], where, theoretically, W-R stars are not expected to form (Maeder 1991)! Indeed, W-R features are never observed in the most metal-poor systems as evidenced from Figure 15, which makes the binary nature of the W-R/non–W-R classification system inappropriate. In

order to correct for this bias, we have compared the W-R and non–W-R samples including only galaxies with $12 + \log (O/H) > 7.6$. In this case (again excluding NGC 5253), *the mean and error-of-the-mean for the two subsamples is identical*, -1.410 ± 0.016 for 20 W-R galaxies and -1.418 ± 0.015 for 37 remaining non–W-R galaxies. It is clear that, for systems with $12 + \log (O/H) > 7.6$, there is no difference between W-R and non–W-R galaxies. The fact that excluding very low-metallicity non–W-R galaxies makes a difference implies that there is a gradual increase in N/O with O/H, consistent with the idea of an increasing contribution from secondary N at higher O/H. This conclusion differs from that drawn by Garnett (1990) who used a much smaller data set and found a trend consistent with constant N/O as a function of O/H.

In Figure 16 we plot He/H versus $12 + \log$ O/H for the same sample of galaxies. The mean He/H for the W-R sample is 0.0861 ± 0.0010 compared to 0.0850 ± 0.0009 for the non–W-R sample, which indicates that the two subsamples are consistent with one another, within 1 σ. If T1004−296, which has the highest He/H, is removed from consideration, the two samples look even more identical. Considering only systems with $12 + \log (O/H) > 7.6$ does not change the conclusion in any way. W-R galaxies do not appear to be preferentially enriched in helium.

While higher quality spectra of many galaxies would be desired, the present data are consistent with W-R galaxies being insignificantly different, on the average, from their non–W-R counterparts. A possible bias might be introduced in the sense of classifying galaxies with W-R stars as non–W-R galaxies since systems observed with narrow slits or at low S/N may actually exhibit W-R features that have been missed or lost in the noise. Even so, the size of the present sample is large enough that we conclude there is not sufficient evidence to treat W-R galaxies differently for purposes of chemical evolution studies. These findings are in agreement with those of Olive & Steigman (1995) who found that the He mass fractions in a sample of W-R, possible W-R, and non–W-R galaxies drawn from the list of Pagel et al. (1992) differ only at the 1 σ level ($\Delta Y_p = 0.002$–0.005.)

6. CONCLUSIONS AND FUTURE WORK

We have measured O, N/O, and He/H abundances at 82 distinct, $2''.1 \times 2''.3$ (43 pc × 47 pc) spatial locations covering almost 400 arcsec^2 in the bright emission-line regions of the Magellanic irregular NGC 4214. We find no localized N/O or He/H abundance irregularities of the sort seen in NGC 5253, and there are no differences between regions showing spectral signatures of Wolf-Rayet stars and the galaxy at large. We do find abundance differences on a larger (200 pc) scale. The southernmost, and apparently youngest, emission-line region (which we have designated Knot 5) exhibits a higher oxygen (and Ne) abundance by 0.1 dex than the rest of the galaxy. The N/O ratio is correspondingly 0.1 dex lower in this region. We have shown that temperature and ionization effects cannot be the cause of the measured differences, and we suggest that recent oxygen pollution from supernovae has occurred in this very young population of massive stars. The means by which O-rich ejecta could cool and mix on timescales comparable to that of the H II regions require further theoretical development.

We have recomputed O, N/O, and He/H abundances for 72 measurements of 60 galaxies with published emission-line strengths in order to compile a self-consistent abundance database. A subsample of galaxies with W-R features exhibits marginally higher N/O ratios (1.5 σ) than a subsample without W-R features. There is no difference between the two subsamples if galaxies with extremely low metallicity (where W-R stars are not expected to form) are

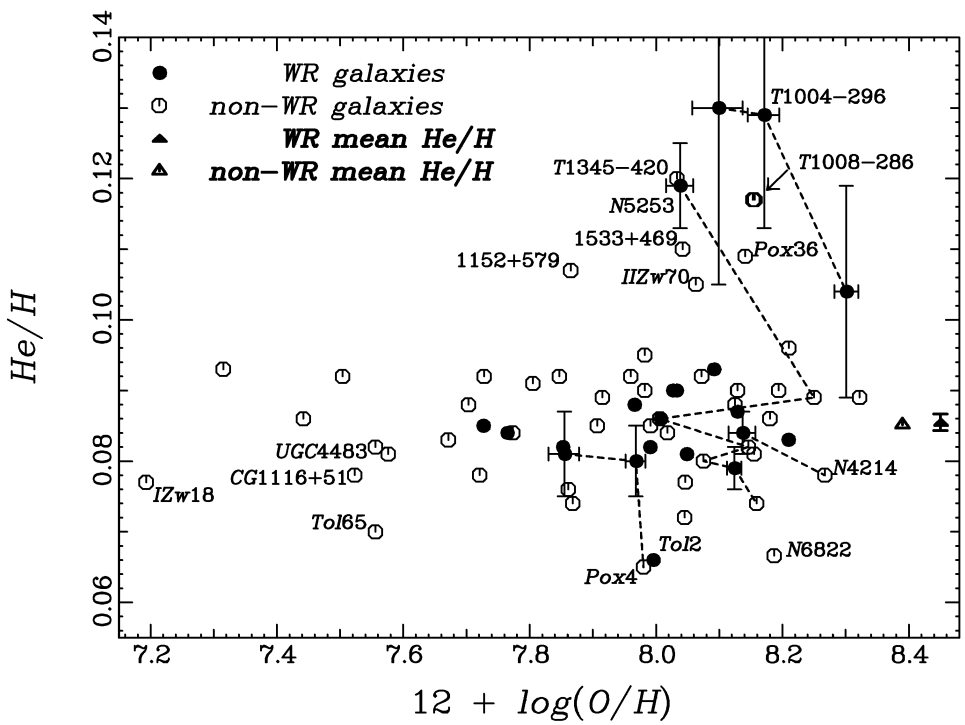

FIG. 16.—He/H vs. $12 + \log$ (O/H) for 72 measurements of 60 low-metallicity galaxies from the literature. Triangles mark the average values of He/H for galaxies with and without W-R features when T1004−296 is removed from the sample. The difference between the two subsamples is negligible.

excluded, which implyies an increase in N/O with O/H, which stands in contrast to previous findings. Comparison of theoretical models of O and N abundance evolution with measured variations at different spatial locations in NGC 5253, NGC 4214, and NGC 3125 is consistent with ongoing O pollution in these systems. Further studies should consider linking the N/O and other chemical abundance ratios with additional starburst age indicators such as EW(Hβ) and the radio continuum spectral index. Based on the present survey of NGC 4214 and a retabulation of abundance data in W-R and non–W-R galaxies, the presence of W-R features alone is not enough to warrant rejecting W-R galaxies from samples used to study chemical evolution or primordial abundances. If localized abundance enrichments do occur, they are evidently not traced by obvious abundance inhomogeneities or the presence of W-R stars.

We would like to thank Deidre Hunter for providing the Hα and continuum images used in Figure 1 and Bill Vacca for helpful comments. We are grateful for many productive conversations with Don Garnett and suggestions from Bernard Pagel. We wish to thank the referee (Manuel Peimbert) for a thorough reading of the manuscript and a number of very helpful comments. E. D. S. appreciates support from NASA LTSARP grant NAGW-3189. H. A. K. is supported by a NASA Graduate Student Researchers Program fellowship. This research has made use of the NASA/IPAC extragalactic database (NED).

APPENDIX

ABUNDANCE COMPILATION FROM THE LITERATURE

We have collected from the literature a large representative sample of spectroscopic measurements in metal-poor galaxies ($12 + \log$ O/H $< \sim 8.4$) and have recomputed the O, N/O, and He/H abundances in a self-consistent manner using the procedure described in § 3. To be eligible for inclusion in our summary, a published data set must include raw or dereddened line strengths for at least the Balmer series, [O II] λ3727, [O III] λ4363, [O III] λ5007, He I λ5876, and [N II] λ6584 with a spectral resolution better than ~ 8 Å in order to separate [N II] λ6584 from Hα. Observations without published uncertainties for the emission-line strengths have been excluded. In computing abundances, we start with the raw line fluxes and derive c(Hβ) and T_e and associated uncertainties. Where only dereddened line strengths are given, we adopt the published c(Hβ). We tabulate the abundance data in Table 5, along with the original reference and footnotes describing the procedure used in each case. For objects with redshift between 0.0030 and 0.0045, we use He I λ6678, when possible, instead of He I λ5876 to compute He abundances.

While the tabulated galaxies do not represent an exhaustive compilation, we have included the majority of spectroscopic surveys of H II galaxies and a few smaller works without any particular bias other than easy access to line strengths and uncertainties. Some galaxies with multiple data sets (II Zw 40 for instance) appear more than once in the table in order to give a feel for observational and systematic errors and possible spatial variations. For some systems with measurements at different spatial locations (NGC 5253, NGC 4214), we tabulate several values, noting the presence or absence of W-R features at each location within the galaxy. For galaxies with multiple measurements that fall within the uncertainties of each other, we have computed a weighted mean for the galaxy as a whole and included that in Table 5. In Figure 15 we have plotted only a single point for most galaxies, representing the weighted mean in the case of multiple measurements. Systems that show strong evidence for internal variations (NGC 5253, Pox 4, NGC 3125, and NGC 4214) are given multiple points connected by a dashed line. Galaxies (and individual locations within a galaxy) showing W-R features are plotted with filled symbols. Data on the presence of W-R features is taken from either the spectroscopy references or the compilation of Kunth & Joubert (1985). We have been conservative in not granting W-R status to galaxies such as Mrk 36, Mrk 5 (Conti 1991), and NGC 4214 Knot 5 (this work), where *narrow* He II λ4686 is seen but clear signs of broad W-R features are not observed.

The compilation presented here is intended as a resource of abundance data in low-metallicity systems derived using current atomic data and realistic, consistent treatment of uncertainties. There are, of course, systematic uncertainties inherent in each data set that are not possible to quantify. Blind use of data from Table 5 for chemical evolution or primordial abundance analyses requiring high precision is not recommended without careful consideration and selective editing. Specifically, tabulated helium abundances have not been corrected for collisional excitation effects in H and He, which are expected to be on the order of 1%–2% at low electron temperatures and densities (Clegg 1987; Skillman et al. 1994).

REFERENCES

Anders, E., & Grevesse, N. 1989, Geochim. Cosmochim. Acta, 53, 197
Allsop, N. J. 1979, MNRAS, 184, 397
Becker, R., Henkel, C., Bomans, D. J., & Wilson, T. L. 1995, A&A, 295, 302
Campbell, A., Terlevich, R., & Melnick, J. 1986, MNRAS, 223, 811
Carigi, L., Colin, P., Peimbert, M., & Sarmiento, A. 1995, ApJ, 445, 98
Clegg, R. A. S. 1987, MNRAS, 229, 31P
Conti, P. S. 1991, ApJ, 377, 115
Conti, P. S., Garmany, C. D., de Loore, C., & Vanbeveren, D. 1983, ApJ, 274, 302
Cunha, K., & Lambert, D. L. 1994, ApJ, 426, 170
De Robertis, M. M., Dufour, R. J., & Hunt, R. W. 1987, JRASC, 81, 195
Dufour, R. J. 1984, in Future of Ultraviolet Astronomy Based on Six Years of *IUE* Research, ed. J. Mead, R. Chapman, & Y. Kondo (Washington: NASA), 107
Dufour, R. J., Schiffer, F. H., & Shields, G. A. 1984, in Future of Ultraviolet Astronomy Based on Six Years of *IUE* Research, ed. J. Mead, R. Chapman, & Y. Kondo (Washington: NASA), 111
Esteban, C., & Peimbert, M. 1995, A&A, 300, 78
Esteban, C., & Vílchez, J. M. 1992, ApJ, 390, 536
Esteban, C., Vílchez, J. M., Manchado, A., & Edmunds, M. G. 1990, A&A, 227, 515
Filippenko, A. V. 1982, PASP, 94, 715
French, H. B. 1980, ApJ, 240, 41
Garnett, D. R. 1989, ApJ, 345, 282
———. 1990, ApJ, 363, 142
Garnett, D. R., & Chu, Y. H. 1994, PASP, 106, 626
Garnett, D. R., & Shields, G. A. 1987, ApJ, 317, 82
Garnett, D. R., Skillman, E. D., Dufour, R. J., Peimbert, M., Torres-Peimbert, S., Terlevich, E., Terlevich, R. J., & Shields, G. A. 1995, ApJ, 443, 64
Howarth, I. D. 1983, MNRAS, 203, 301
Hummer, D. G., & Storey, P. J. 1987, MNRAS, 224, 801
Humphreys, R. M., Nichols, M., & Massey, P. 1985, AJ, 90, 101
Hunter, D. A. 1996, private communication

Izotov, Y., Thuan, T. T., & Lipovetsky, V. A. 1994, ApJ, 435, 647
Kinman, T. D., & Davidson, K. 1981, ApJ, 243, 127
Kobulnicky, H. A., & Skillman, E. D. 1996, in preparation
Kunth, D., & Joubert, M. 1985, A&A, 142, 411
Kunth, D., & Sargent, W. L. W. 1983, ApJ, 273, 81
———. 1986, ApJ, 300, 496
Leitherer, C., Conti, P. S., Vacca, W. D., Filippenko, A. V., Carmelle, R., & Sargent, W. L. W. 1996, preprint
Lequeux, J., Peimbert, M., Rayo, J. F., Serrano, A., & Torres-Peimbert, S. 1979, A&A, 80, 155
Maeder, A. 1991, A&A, 242, 93
———. 1992, A&A, 264, 105
Martin, P., & Roy, J. R. 1994, 424, 599
Mathis, J. S., Chu, Y-H., & Peterson, D. 1985, ApJ, 292, 155
Meyer, J. P. 1985, ApJS, 57, 173
Oke, J. B. 1990, AJ, 99, 1621
Olive, K. A., & Steigman, G. 1995, ApJS, 97, 49
Osterbrock, D. E. 1989, Astrophysics of Gaseous Nebulae and Active Galactic Nuclei (Mill Valley: University Science Books)
Pagel, B. E. J., Edmunds, M. G., & Smith, G. 1980, MNRAS, 193, 219
Pagel, B. E. J., Simonson, E. A., Terlevich, R. J., & Edmunds, M. G. 1992, MNRAS, 255, 325
Pagel, B. E. J., Terlevich, R. J., & Melnick, J. 1986, PASP, 98, 1005
Peimbert, M., Sarmiento, A., & Fierro, J. 1991, PASP, 103, 815
Peimbert, M., & Spinrad, H. 1970, A&A, 7, 311
Peimbert, M., & Torres-Peimbert, S. 1974, ApJ, 193, 327
———. 1976, ApJ, 203, 581
Sandage, A., & Bedke, J. 1994, The Carnegie Atlas of Galaxies (Washington: Carnegie Institution of Washington)
Sargent, W. L. W., & Filippenko, A. V. 1991, AJ, 102, 107
Seaton, M. J. 1979, MNRAS, 187, 73P
Searle, L. 1971, ApJ, 168, 327
Searle, L., & Sargent, W. L. W. 1972, ApJ, 173, 25
Shaw, R. A., & Dufour, R. J. 1995, PASP, 107, 896
Skillman, E. D. 1984, Ph.D. thesis, Univ. of Washington
———. 1985, ApJ, 290, 449
———. 1989, ApJ, 347, 883
Skillman, E. D., & Kennicutt, R. C. 1993, ApJ, 411, 655
Skillman, E. D., Terlevich, R. J., Kennicutt, R. C., Garnett, D. R., & Terlevich, E. 1994, ApJ, 431, 172
Smits, D. P. 1996, MNRAS, 278, 683
Stasińska, G. 1990, A&AS, 83, 501
Talent, D. L. 1980, Ph.D. thesis, Rice Univ.
Tenorio-Tagle, G. 1996, AJ, in press
Thuan, T. T., Izotov, Y., & Lipovetsky, V. A. 1995, ApJ, 445, 108
Tinsley, B. 1974, ApJ, 192, 629
———. 1976, ApJ, 208, 797
Tully, R. B. 1988, Nearby Galaxies Catalog (Cambridge: Cambridge University Press)
Villa-Costas, M. B., & Edmunds, M. G. 1993, MNRAS, 265, 199
Walsh, J. R., & Roy, J.-R. 1987, ApJ, 319, L57
———. 1989, MNRAS, 239, 297
———. 1993, MNRAS, 262, 27
Welch, G. A. 1970, ApJ, 161, 821